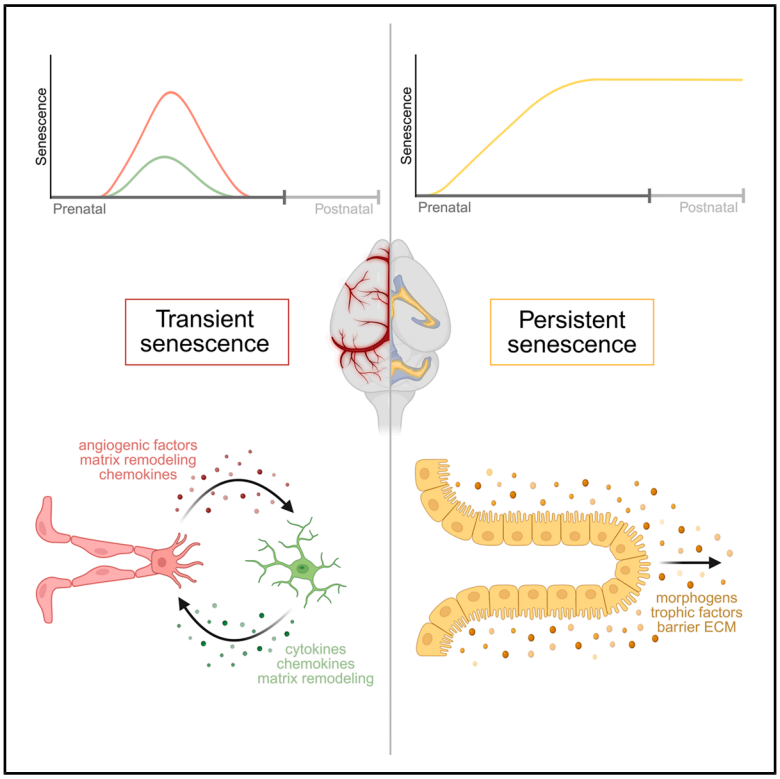
Cell

Persistent and transient senescent cells contribute to brain-barrier development

Graphical abstract



Authors

L. Ashley Watson, Zoe Adelsheim, Mackenzie J. Carter, ..., Rania H. Palaniappan, John M. Augustine, Hiruy S. Meharena

Correspondence

hmeharena@ucsd.edu

In brief

Senescent cell states arise across brain-barrier cell types during development but diverge in duration and function. Endothelial cells and macrophages enter a transient, inflammatory state, whereas choroid plexus epithelial cells maintain a persistent, non-inflammatory state supporting long-term barrier function. These cells are required for brain-barrier formation and function.

Highlights

- Distinct senescent states arise across brain-barrier cell lineages
- Endothelial cells and macrophages engage a transient inflammatory senescent state
- Choroid plexus epithelium maintains a persistent non-inflammatory senescent state
- Senescent cell ablation alters vascular patterning and CSF homeostasis

Watson et al., 2026, Cell *189*, 1–15
July 9, 2026 © 2026 The Authors. Published by Elsevier Inc.
https://doi.org/10.1016/j.cell.2026.05.022

CellPress

Please cite this article in press as: Watson et al., Persistent and transient senescent cells contribute to brain-barrier development, Cell (2026), https://doi.org/10.1016/j.cell.2026.05.022

Cell

CellPress
OPEN ACCESS

Article

Persistent and transient senescent cells contribute to brain-barrier development

L. Ashley Watson,[1] Zoe Adelsheim,[1,4] Mackenzie J. Carter,[1,4] Grace T. Carter,[1] Karen L. Jimenez-Reyes,[1] Huijie Du,[1] Ziqing Zhu,[1] David B. Berry,[2] Mia C. Paredez,[1] Rania H. Palaniappan,[1] John M. Augustine,[1] and Hiruy S. Meharena[1,3,5,*]
[1]Department of Neurobiology, University of California, San Diego, La Jolla, CA, USA
[2]Department of Orthopedic Surgery, University of California, San Diego, La Jolla, CA, USA
[3]Department of Molecular Biology, University of California, San Diego, La Jolla, CA, USA
[4]These authors contributed equally
[5]Lead contact
*Correspondence: hmeharena@ucsd.edu
https://doi.org/10.1016/j.cell.2026.05.022

SUMMARY

Establishment of the blood-brain barrier (BBB) and blood-cerebrospinal fluid (CSF) barrier requires precise coordination between diverse cell types to protect and nourish the brain. Here, we identify developmentally programmed p21$^+$ senescent cells that exhibit divergent senescence-associated features across these two brain interfaces in mice. In the choroid plexus (ChP), epithelial cells adopt a lifelong, non-inflammatory senescent state associated with CSF production and blood-CSF barrier integrity. In contrast, vascular endothelial cells and brain-resident macrophages transiently exhibit pro-inflammatory senescence profiles during brain vascularization, with reciprocal signaling linked to angiogenic patterning and extracellular matrix assembly. The ablation of p21$^+$ cells during mid-gestation disrupts brain vascular patterning and ChP integrity, which results in hemorrhage, impaired CSF production, and ventricular collapse. These findings indicate that embryonic senescent cells adopt divergent transient and long-lived states that support brain-barrier formation and homeostasis, thus reframing the prevailing view of persistent senescence beyond solely a pathological state.

INTRODUCTION

Cellular senescence is a multifaceted program with roles in development, aging, and disease.[1,2] While traditionally viewed as a stress-responsive growth arrest, it is increasingly recognized as a physiological mechanism in development and regeneration.[3–5] During embryogenesis, transient senescent cells contribute to tissue remodeling in the limb, kidney, endolymphatic sac, and placenta.[3,4,6] These cells exhibit canonical hallmarks, including cyclin-dependent kinase inhibitor 1 (*Cdkn1a*/p21) expression, cell-cycle arrest, lysosomal dysfunction, and a senescence-associated secretory phenotype (SASP), which enables them to influence local environments independent of proliferation or apoptosis.[1,2,7] Through SASP, they secrete factors that remodel tissue environments and influence neighboring cell behavior.[3,4,7,8] In the brain, by contrast, cellular senescence has been associated with aging and neurodegeneration, where it contributes to cognitive decline.[9,10] Additionally, emerging evidence implicates cellular senescence in neurodevelopmental disorders, which includes autism spectrum disorder (ASD), microcephaly, and Down syndrome (DS).[1,11–13] However, whether senescence-associated cell states are a component of normal neurodevelopment remains unclear.

Brain morphogenesis requires a series of spatially and temporally coordinated events that generate diverse cell types and specialized structures critical for its function. Neuroepithelial cells of the neural tube give rise to neurons, astrocytes, oligodendrocytes, ependymal cells, and choroid plexus epithelial (ChPe) cells of the brain.[14,15] During mid-gestation, invasion of the neural tube by vascular endothelial cells (VECs), macrophages, and pericytes facilitates the establishment of the blood-brain barrier (BBB), a structure that protects neural tissue and regulates the delivery of nutrients and signaling molecules from the blood.[16–18] Simultaneously, the neural tube gives rise to the long-lived choroid plexus (ChP), a structure composed primarily of epithelial cells.[19–22] The ChP forms the blood-cerebrospinal fluid (CSF) barrier and is responsible for the production of CSF, a fluid critical for brain development, homeostasis, and waste clearance.[15,19,20,23,24] Although the molecular and cellular processes driving BBB and blood-CSF barrier formation are well studied, it remains unclear whether specific subsets of barrier-forming cells adopt analogous, cell-type-specific functional states that collectively contribute to barrier development.

Here, we identify developmentally programmed p21$^+$ senescent cell populations linked to brain-barrier formation and function. During mid-gestation, senescent cells emerge in three key populations of the mouse brain: ChPe cells, VECs, and brain-resident macrophages. These cells display classical senescence hallmarks, including a shared transcriptional signature, SASP, lysosomal dysfunction, and cell-cycle exit. In addition to these

This is an open access article under the CC BY license (http://creativecommons.org/licenses/by/4.0/).

Please cite this article in press as: Watson et al., Persistent and transient senescent cells contribute to brain-barrier development, Cell (2026), https://doi.org/10.1016/j.cell.2026.05.022

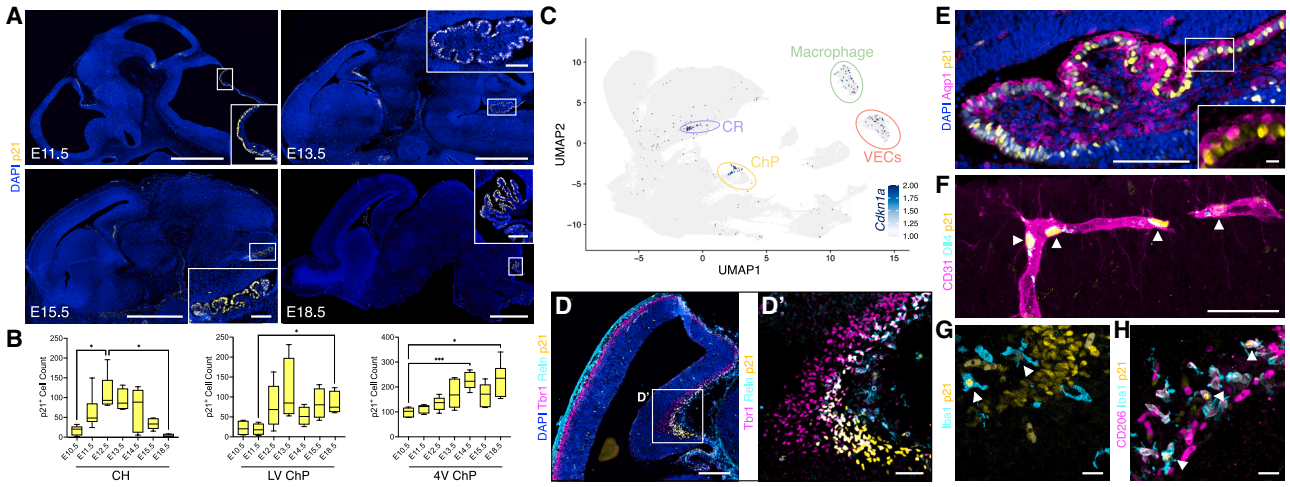


Figure 1. p21 is expressed in Cajal-Retzius (CR) cells, choroid plexus epithelial (ChPe) cells, vascular endothelial cells (VECs), and brain-resident macrophages during embryonic development

(A) p21 (yellow) and DAPI (blue) in E11.5–E18.5 mouse brain. Scale bars, 1 mm and 100 μm (inset).

(B) Quantification of $p21^+$ cells in cortical hem (CH), lateral ventricle (LV), and 4th ventricle (4V) choroid plexus (ChP); n = 3–4 biological replicates/timepoint. Mean ± min. and max. values.

(C) Uniform manifold approximation and projection (UMAP) of 283,323 cells from E8.0–E18.0 mouse brain, with *Cdkn1a* expression (blue).

(D–H) p21 (yellow) with lineage markers: (D) Tbr1 (magenta) and Reln (cyan) at E13.5. Scale bars, 200 μm and 50 μm (D'). (E) Aqp1 (magenta) in E13.5 LV ChP. Scale bars, 100 μm and 10 μm (inset). (F) Dll4 (cyan) and CD31 (magenta) in E15.5 cortex. Scale bar, 20 μm. (G) Iba1 (cyan) in E13.5 CH. Scale bar, 20 μm. (H) CD206 (magenta) and Iba1 (cyan) in E15.5 cortex. Scale bar, 20 μm. *$p < 0.05$, **$p < 0.01$, and ***$p < 0.001$ by Brown-Forsythe and Welch's one-way ANOVA with multiple comparisons.

See also Figure S1; Tables S1 and S2.

shared features, each cell type displays distinct molecular profiles and functional roles. In ChPe cells, senescence is characterized by a non-inflammatory secretory state and upregulation of epithelial and barrier-related genes. Remarkably, this state persists into adulthood, which suggests that it can contribute to the specialized, non-renewing functions of epithelial barrier cells. In contrast, VECs and brain-resident macrophages enter a transient embryonic senescent state marked by inflammatory SASP, enriched receptor-ligand interactions, and coordinated angiogenic patterning and extracellular matrix (ECM) deposition. Using both pan- and cell-type-specific ablation of $p21^+$ cells *in vivo*, we dissect the contributions of these populations to brain development. Pan-lineage $p21^+$ ablation reveals that these cells are collectively important for vascular patterning, ChP integrity, and CSF regulation, whereas macrophage-specific $p21^+$ ablation highlights a selective role in supporting vascular morphogenesis. Our findings support a model in which embryonically programmed senescent cell states occur in the brain in temporally distinct modes, with transient states contributing to developmental remodeling and vascular patterning, and persistent states supporting the lifelong maintenance of ChP structure and function.

RESULTS

Spatiotemporal expression of p21 in specialized brain cell types during neurodevelopment

Elevated expression of p21 is a hallmark of cellular senescence, which includes programmed embryonic senescence during mid-gestation.[3,4] In sequential sagittal cryosections from whole embryonic day (E) 13.5 mouse embryos (Figure S1A; Video S1), we identified that $p21^+$ cells were highly abundant in the developing ChP of the lateral ventricle (LV) and fourth ventricle (4V), and in the adjacent cortical hem region, as they appeared in over 80% of tissue sections (Figure S1B). All three regions showed enrichment of $p21^+$ cells with distinct temporal patterns between E10.5–E18.5 (Figures 1A and 1B). In the cortical hem, the number of $p21^+$ cells peaked at E12.5–E13.5 and disappeared by E18.5. In contrast, $p21^+$ cells in the LV and 4V ChP peaked at E13.5–E14.5 and remained elevated at later stages. We also observed scattered $p21^+$ cells outside these high-density regions across all time points (Figures S1C–S1F).

To identify the specific brain cell types that express p21 during neurodevelopment, we utilized a previously published single-cell RNA-sequencing dataset (scRNA-seq)[25] spanning E8–E18 of the developing mouse brain. Of the 51 transcriptionally distinct clusters (Table S1), four had a significant proportion (>10%) that expressed *p21* (*Cdkn1a*) (Figure 1C; Table S2). This included Cajal-Retzius (CR) cells (*Trp73*, *Reln*, *Calb2*, and *Tbr1*), ChPe cells (*Cfap126*, *Cfap52*, *Pifo*, and *Foxj1*), VECs (*Ly6c1*, *Cldn5*, *Flt1*, and *Pecam1*), and brain-resident macrophages (*Trem2*, *Aif1*, *Spi1*, *Csf1r*, *Mrc1*, and *P2ry12*) (Figures S1G–S1J). We confirmed p21 expression in T-box brain transcription factor ($Tbr1^+$) CR cells in the embryonic cortical hem (Figure 1D), aquaporin-1 ($Aqp1^+$) ChPe (Figure 1E), cluster of differentiation 31 ($CD31^+$) endothelial cells that frequently co-expressed delta-like canonical notch ligand 4 ($Dll4^+$; Figure 1F), and both

Please cite this article in press as: Watson et al., Persistent and transient senescent cells contribute to brain-barrier development, Cell (2026), https://doi.org/10.1016/j.cell.2026.05.022

Iba1$^+$ microglia in the brain parenchyma (Figure 1G) and Iba1$^+$/CD206$^+$ border-associated macrophages (BAMs; Figure 1H).

Embryonic p21$^+$ brain cell types exhibit hallmarks of cellular senescence

Cell-cycle arrest in senescent cells is predominantly accomplished through the upregulation of cyclin-dependent kinase (CDK) inhibitors p21 and p16.[26] However, embryonic senescence is p21-dependent and p16-independent.[3,4] Consistent with this, *Cdkn2a* (p16)-expressing cells were not detected in the embryonic brain scRNA-seq dataset (Figure S1K), and subsequent analyses therefore focused on p21$^+$ cells. Since p21 is not a specific marker of cellular senescence,[3,4,27–29] and no single marker defines this state,[30,31] we used a multidimensional approach to characterize whether the p21$^+$ embryonic brain cell types are indeed senescent. We first defined a senescence-associated transcriptional signature (SaTS) using established *in vitro* models of mouse cellular senescence, including those induced by ionizing radiation (IR), doxorubicin (DOX), replicative exhaustion (REP), or oncogene-induced senescence (OIS; Figure S2A; Table S3).[32,33] Across these models, we observed a shared gene expression pattern marked by the downregulation of cell-cycle, DNA-replication, and protein-translation genes (1,315 genes), and the upregulation of inflammatory-response, lysosome-function, cytokine-production, lipid-catabolism, and vesicular-transport genes (1,203 genes; Figures S2B and S2C; Table S3). The signatures showed strong directional concordance with established senescence gene sets[34,35] (Figure S2D; Table S3), which confirmed that SaTS captures the core transcriptional features of cellular senescence.

We next compared p21$^+$ transcriptional programs to SaTS in a cell-type-specific manner. For neuroepithelial lineage cells (CR and ChPe), we compared p21$^+$ cells to their progenitors, and for VECs and brain-resident macrophages, cell types that originate outside of the brain, we compared p21$^+$ to p21$^-$ cells. Next, we performed a permutation test (10,000 randomized permutations) to assess whether the differentially expressed genes (DEGs) identified in p21$^+$ cells are similar to SaTS. Across all cell types, p21$^+$ cells showed significant transcriptional similarity to senescent cells, with a strong directional correlation ($p < 10^{-4}$) between the up- and downregulated genes identified in the p21$^+$ populations and SaTS (Figures 2A and S2E). Analysis of shared SaTS genes revealed that downregulated genes were broadly conserved across all four p21$^+$ cell types, thus supporting a common suppression of proliferative and translational programs (Figure S2F). Consistent with this program, p21$^+$ cells downregulated genes related to cell cycle and protein translation (Figure 2B), p21$^+$ cells lacked expression of Ki67 (Figures 2C–2H and S2G), and p21$^+$ ChPe cells had reduced protein synthesis (Figures S2H and S2I). In canonical *in vitro* models, DNA damage is a key upstream trigger of p21-mediated senescence.[2] However, similar to previous reports of embryonic senescence,[3,4] we found no evidence of DNA damage or apoptosis in p21$^+$ cells (Figures S2J–S2M).

The upregulated SaTS genes exhibited substantial cell-type specificity, with p21$^+$ VECs and macrophages enriched for immune-associated signatures, VECs and ChPe cells enriched for lipid-catabolism genes, CR cells enriched for vesicle-mediated transport and endoplasmic reticulum organization, and ChPe cells uniquely enriched for cilia and galactosidase activity genes (Figure S2F). We investigated lysosomal dysfunction, a hallmark of senescence characterized by increased SA-β-galactosidase (SA-β-gal) activity at pH 6.0[36] and lipofuscin accumulation.[37] All four p21$^+$ cell types transcriptionally upregulated lysosomal genes (Figure 2B); however, the functional markers of lysosomal dysfunction, SA-β-gal and lipofuscin, were only present in p21$^+$ ChPe cells, VECs, and macrophages and were absent in CR cells (Figures 2I–2M and S2N).

Additionally, p21$^+$ ChPe cells, VECs, and macrophages, but not CR cells, upregulated key SASP-related pathways such as cytokine production and secretory vesicles (Figure 2B). Accordingly, the upregulated genes in these cell types were enriched for genes encoding secreted factors (Figure S3A; Table S3).[38] To directly assess overlap with SASP, we curated a list of SASP genes defined as secreted factors upregulated in at least one *in vitro* model of cellular senescence (Table S3). Upregulated secreted genes in p21$^+$ VECs, macrophages, and ChPe cells significantly overlapped with the SASP gene set, with 77.3% in p21$^+$ VECs (Fisher's $p = 1.17 \times 10^{-208}$; Figure 2N), 88.5% in p21$^+$ macrophages ($p = 8.33 \times 10^{-80}$; Figure 2O), and 73.4% in p21$^+$ ChPe cells ($p = 5.25 \times 10^{-216}$; Figure 2P), thus supporting the presence of a SASP-like profile. Although the cell types shared some SASP features, each exhibited a distinct secretory signature with upregulated factors involved in shared functional modules such as ECM remodeling, cell communication, and angiogenesis (Figures S3B–S3E). p21$^+$ macrophages upregulated a strong pro-inflammatory profile, which included canonical cytokines and chemokines such as *Il1a/b*, *Il6*, *Tnf*, and *Ccl2/3/4/7* (Figures 2Q and S3C). p21$^+$ VECs displayed a partially overlapping inflammatory signature characterized by *Cxcl1/2*, *Mmp9*, and *Isg15* expression (Figures 2N and S3D). In contrast, p21$^+$ ChPe cells upregulated a distinct set of trophic secreted factors, 92% of which overlap with the most abundant factors enriched in the embryonic CSF[39] ($p = 2.2 \times 10^{-16}$), which includes *Igf2*, *Apoe*, *Adamts1*, and *Timp3* (Figures 2N, S3E, and S3F), thus pointing to divergent signaling across cell types.

Together, these findings demonstrate that embryonic p21$^+$ ChPe cells, VECs, and brain-resident macrophages exhibit key hallmarks of cellular senescence, whereas CR cells do not (Table 1). While vascular and immune populations exhibited a classical pro-inflammatory SASP, ChPe cells adopt a distinct secretory transcriptional profile tailored to their functional output. In contrast, p21$^+$ CR cells displayed a similar transcriptional state but lacked the cellular hallmarks of senescence. In fact, genes upregulated in p21$^+$ CR cells were involved in neuronal differentiation and migration (Figure S3G), and p21 expression within the cortical hem was inversely correlated with mature CR markers Tbr1 and Reln (Figures 1D and S3H), which suggests that transient p21 expression in these cells plays a role in differentiation[28] rather than a bona fide senescent state.

Spatiotemporal dynamics of embryonic senescence in the brain

While we identified p21$^+$ senescent cells in epithelial, immune, and vascular compartments, their developmental trajectories remained unknown. We generated an inducible lineage tracing

Please cite this article in press as: Watson et al., Persistent and transient senescent cells contribute to brain-barrier development, Cell (2026), https://doi.org/10.1016/j.cell.2026.05.022

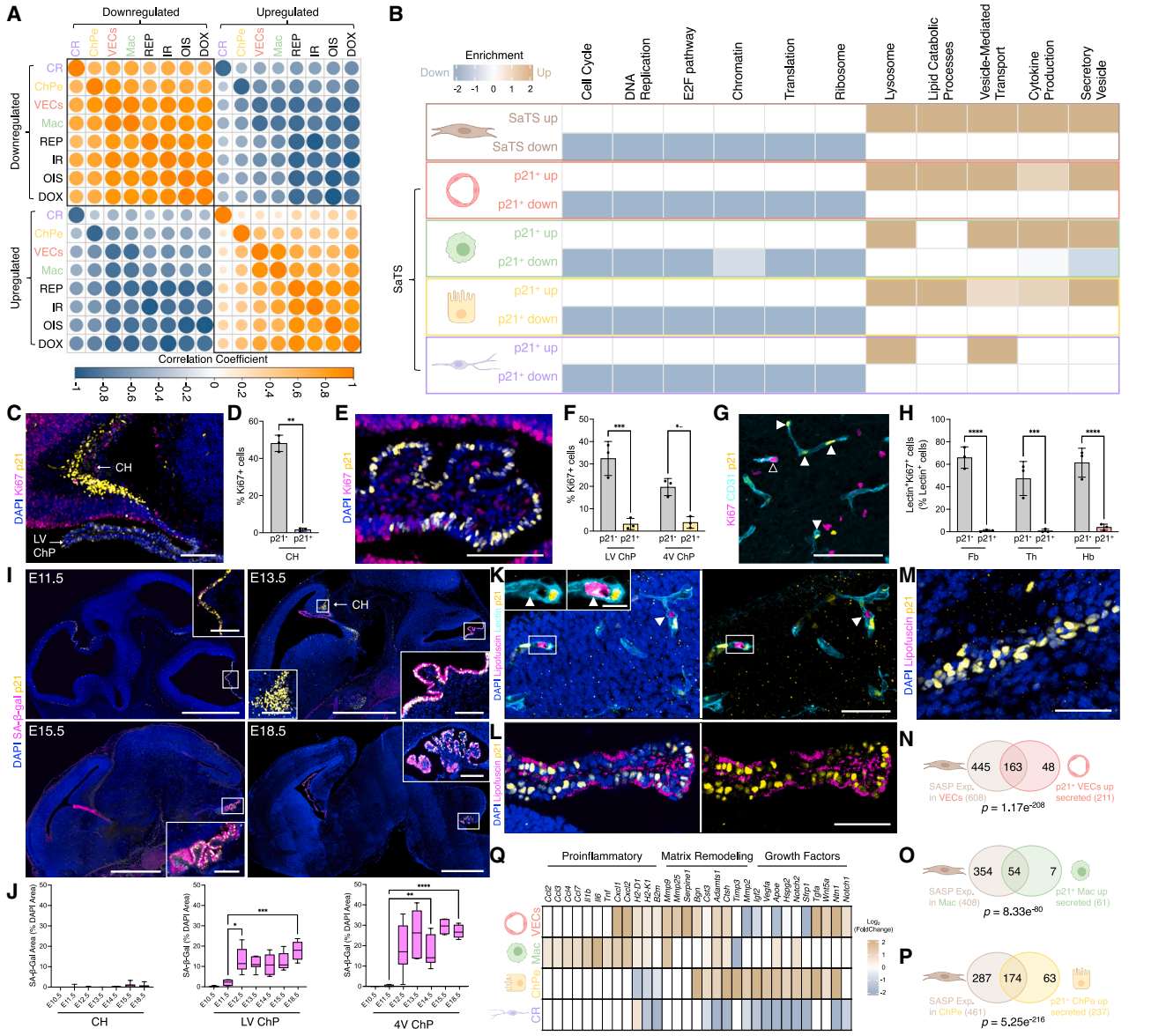


Figure 2. p21⁺ ChPe cells, VECs, and brain-resident macrophages exhibit hallmarks of senescence

(A) Correlation of senescence (DOX, OIS, IR, or REP) with p21⁺ CR, ChPe, VEC, and brain-resident macrophage (Mac) cell transcriptional signatures.

(B) Gene Ontology (GO) enrichment of SaTS and shared genes.

(C–H) Ki67 (magenta) and p21 (yellow) staining and quantification in E12.5 CH (C), E12.5 ChP (E), and E15.5 thalamus (G); $n > 100$ cells, 3 replicates. Scale bars, 100 μm (C) and (E) and 50 μm (G).

(I and J) p21 (yellow) and SA-β-gal (magenta) in E11.5–E18.5 and quantification (percentage DAPI) in CH, LV, and 4V ChP; $n = 3$–4 replicates. Scale bars, 1 mm and 100 μm (inset).

(K) p21 (yellow), lectin (cyan), and lipofuscin (magenta) in E15.5 cortex. (Inset) Single z. Scale bars, 50 μm and 10 μm (inset).

(L) p21 (yellow) and lipofuscin (magenta) in E15.5 LV ChP. Scale bar, 50 μm.

(M) p21 (yellow) and lipofuscin (magenta) in E15.5 CH. Scale bar, 50 μm.

(N–P) Overlap of SASP factors across cell types.

(Q) SASP gene $\log_2$fold-change heatmap in p21⁺ cells. *$p < 0.05$, **$p < 0.01$, ***$p < 0.001$, and ****$p < 0.0001$ by unpaired two-tailed Student's t test (D), two-way ANOVA followed by Šídák's multiple comparisons test (F) and (H), Brown-Forsythe and Welch's one-way ANOVA with multiple comparisons (J), or hypergeometric test (N)–(P). Data are represented as mean ± SD (D), (F), and (H) or mean ± min. and max (J).

See also Figures S2 and S3; Table S3.

Please cite this article in press as: Watson et al., Persistent and transient senescent cells contribute to brain-barrier development, Cell (2026), https://doi.org/10.1016/j.cell.2026.05.022

Table 1. p21⁺ ChPe cells, VECs, and brain-resident macrophages exhibit core features of senescence

Senescence hallmark	CR	ChPe	Macrophage	VECs
Transcriptional signature	✓	✓	✓	✓
Cell cycle arrest/exit	✓	✓	✓	✓
Lysosome: SA-β-gal/lipofuscin	–	✓	✓	✓
SASP	–	✓	✓	✓

Summary of findings from analysis of core senescence features in embryonic p21⁺ Cajal-Retzius (CR) cells, ChPe cells, brain-resident macrophages, and vascular endothelial cells (VECs).

system by placing a tamoxifen-responsive Cre recombinase (Cre-ERT2-2A) downstream of the *Cdkn1a*/p21 promoter (*p21-CreERT2*). Crossed with the Ai9 reporter mice,[40] this system enables temporal labeling of p21-expressing cells with tdTomato (tdT) following tamoxifen exposure (Figure S4A). In the absence of tamoxifen, we did not detect any tdT⁺ cells, thus confirming the specificity of our system (Figure S4B). Daily tamoxifen injection between E11.5–E15.5 labeled a substantial proportion of p73⁺ CR cells (~80%–90%), ChP cells (~80%–90%), and lectin⁺ vasculature (~60%–80%) at E18.5 (Figures S4C–S4E). In contrast, we observed that only ~15%–20% of Iba1⁺ brain-resident macrophages were tdT⁺ at E18.5 (Figure S4F).

To gain a better understanding of the spatiotemporal dynamics of senescence entry, we performed tamoxifen injections across three developmental windows representing early (E9.5–E11.5), mid- (E12.5–E13.5), or late- (E14.5–E15.5) mid-gestational phases and assessed tdT⁺ cells at E18.5 and postnatal day 21 (PND21; Figure S4G). At PND21, we detected tdT⁺ cells distributed throughout the brain, with an increased frequency in the mid- and late-injection windows (Figure S4H). tdT⁺ cells displayed diverse morphologies, including neuronal, macrophage, vascular, and epithelial types (Figure S4I), which is consistent with immunostaining and scRNA-seq analysis (Figure 1).

We validated the lineage tracing system using CR cells, which exhibit well-defined temporal dynamics.[41,42] At E18.5, tdT⁺/p73⁺ cells were identified in both cortical and hippocampal marginal zones (Figures S4J and S4L) and expressed Reln (Figure S4M). As expected, cortical CR cells were absent by PND21, whereas hippocampal tdT⁺/p73⁺ cells remained (Figures S4K and S4L), thus recapitulating the known temporal patterns of CR cell genesis and confirming that our system reliably captures regionally and temporally accurate p21 expression during brain development.

Analysis across early, mid, and late windows revealed distinct temporal expression of p21⁺ cells across ChPe cells, VECs, and brain-resident macrophages. During the early window (E9.5–E11.5), labeling was sparse in most lineages (Figures 3B, 3E, and 3G). In the ChP, tdT⁺ labeling was detected prior to ChP morphogenesis (~E11.5–E12.5)[20] in ~10%–25% of ChPe cells (Figures 3A and 3B), which suggested an early onset of p21 expression in a subset of progenitors. VECs exhibited minimal labeling at this stage (~2%–18% of lectin⁺ area; Figures 3C–3E), which was predominant in the hindbrain, where vascular development initiates earliest (~E10).[43,44] Similarly, p21⁺ brain-resident macrophages (tdT⁺/Iba1⁺) were sparse, with < 5% being detected throughout the brain during the early labeling window (Figures 3F and 3G). These observations indicate that a limited fraction of cells within the brain exhibit senescence-associated p21 expression during early neurodevelopment.

By the mid-window (E12.5–E13.5), p21⁺ cell labeling expanded in all three cell types. ChPe cell labeling rose to ~50% (Figure 3B), which coincided with rapid epithelial expansion and functional maturation. VEC labeling increased in the hindbrain and thalamus (~25%–30%) and remained low in the forebrain (~5%; Figure 3E), thus mirroring the rostrocaudal progression of angiogenesis and initial BBB formation.[44–46] A corresponding rise in labeled brain-resident macrophages in this window was reminiscent of the regional and temporal increase in VEC labeling (Figure 3G). The late window (E14.5–E15.5) captured peak p21 labeling across all lineages. ChPe tdT⁺ labeling remained high (~50%) and at similar levels through PND21 (Figures 3A and 3B) without substantial changes in ChP size (Figure S4N). At PND21, we observed extracellular budding of tdT⁺ LV ChPe cells (Figure S4O), which supports their role in CSF secretion and vesicle-based signaling.[47] Late-window VEC and brain-resident macrophage labeling increased across all three brain regions: VEC labeling in the forebrain, thalamus, and hindbrain rose to ~20%, 40%, and 30%, respectively (Figure 3E), which coincides with ongoing vascular remodeling during BBB maturation.[46,48] tdT⁺ VECs co-expressed the nuclear marker ETS-related gene (ERG) (Figure S4P), thus confirming their endothelial identity. Brain-resident macrophage labeling also peaked during this window to ~10% of Iba1⁺ cells, particularly in the thalamus and hindbrain parenchyma (Figure 3G). Together, these patterns indicate that p21⁺ senescent cells emerge in a spatially and temporally defined manner alongside the development of the brain's barrier systems.

Persistent senescence in the postnatal ChP

Early studies suggested that embryonic senescent cells are transient, as they appear during key developmental windows before immune-mediated clearance.[3,4] However, subsequent lineage tracing studies indicate that some senescent cells can escape clearance, re-enter the cell cycle, and contribute to adult tissues.[49] We failed to detect tdT⁺/EdU⁺ (ethynyl-2′-deoxyuridine-positive) cells that reentered the cell cycle at E12.5 (Figure S4Q). Similarly, tdT⁺ cells labeled during early, mid, or late windows in the forebrain and hindbrain did not express Ki67 at E18.5 (Figures S4R–S4V), which indicated that p21⁺ cells of the brain do not re-enter the cell cycle during embryogenesis. Additionally, LV and 4V tdT⁺ ChPe cells lacked Ki67 at E18.5 and PND21 (Figures S4W and S4X), which aligned with the embryonic origin and low turnover of the ChP.[22]

Lineage tracing showed that most embryonic p21⁺ ChPe cells, VECs, and brain-resident macrophages remain until at least three weeks after birth (Figures 3B, 3E, and 3G), but it is unclear whether these cell types retain senescence markers postnatally. We detected tdT⁺/p21⁺/SA-β-gal⁺ and tdT⁺/p21⁺/lipofuscin⁺ ChPe cells at PND21 following late-window tamoxifen labeling (Figures 4A and 4B). In contrast, neither p21, SA-β-gal, nor lipofuscin were detected in tdT⁺/lectin⁺ VECs or tdT⁺/Iba1⁺ brain-resident macrophages postnatally (Figures 4A and 4B).

Please cite this article in press as: Watson et al., Persistent and transient senescent cells contribute to brain-barrier development, Cell (2026), https://doi.org/10.1016/j.cell.2026.05.022

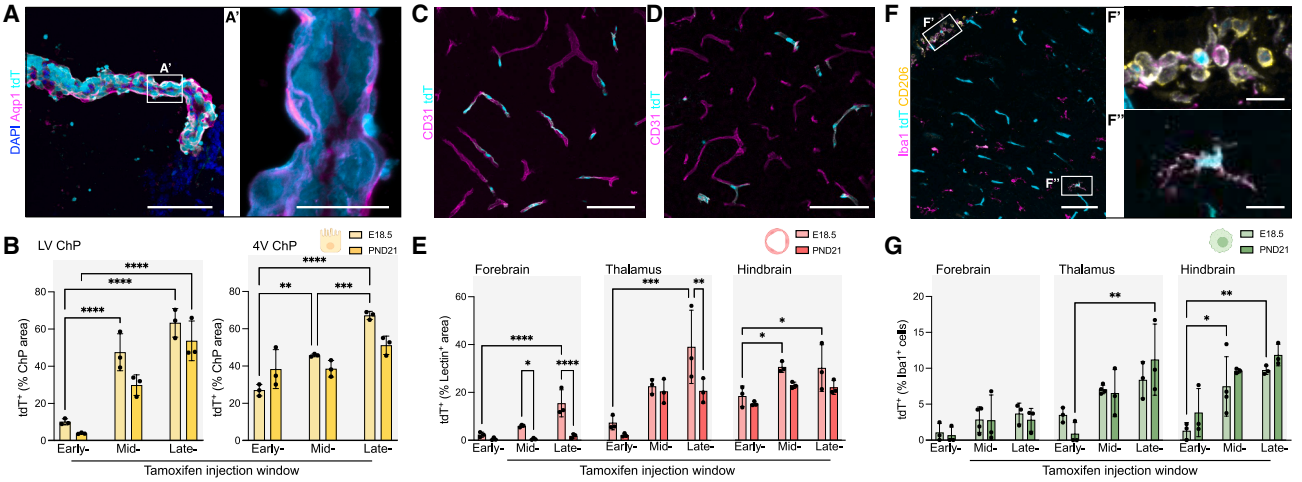


Figure 3. Embryonic p21$^+$ cells emerge in discrete brain regions and are retained into the postnatal period

(A) Aqp1 (magenta) and tdT (cyan) in PND21 LV ChP after late-window tamoxifen labeling. Scale bars, 100 μm and 20 μm (A').

(B) tdT$^+$ cells (percentage ChP DAPI area) in the LV (left) and 4V ChP (right) at E18.5 and PND21, $n = 3$.

(C and D) CD31 (magenta) and tdT (cyan) in E18.5 (C) and PND21 (D) forebrain after late-window tamoxifen labeling. Scale bar, 100 μm.

(E) tdT$^+$ cells (percentage lectin$^+$ area) in forebrain, thalamus, and hindbrain at E18.5 and PND21, $n = 3$.

(F) CD206 (yellow), Iba1 (magenta), and tdT (cyan) in E18.5 midbrain after late-window tamoxifen labeling. Scale bars, 100 μm (F) and 20 μm (F') and (F'').

(G) tdT$^+$ (percentage Iba1$^+$ cells) in forebrain, thalamus, and hindbrain at E18.5 and PND21, $n = 3$. $^*p < 0.05$, $^{**}p < 0.01$, $^{***}p < 0.001$, and $^{****}p < 0.0001$ by two-way ANOVA followed by Tukey's multiple comparisons test.

See also Figure S4.

Moreover, we detected SA-β-gal$^+$/p21$^+$ ChPe cells in a 12-month-old brain (Figure 4C).

Collectively, these findings highlight the divergent spatiotemporal dynamics of embryonic p21$^+$ cells of the brain. While ChPe cells retain senescence markers postnatally, vascular and macrophage populations show transient embryonic senescence during the key stages of BBB development. To investigate how these populations influence barrier development, we next examined their transcriptional profiles, cell-cell interactions, and performed targeted ablation during mid-gestation.

Interplay between embryonic senescent brain-resident macrophages and vascular cells

The transcriptional state of p21$^+$ VECs and brain-resident macrophages revealed shared upregulation of SASP-related pathways, including inflammation, cytokine signaling, and angiogenesis (Figures 5A and 5B). p21$^+$ brain-resident macrophages upregulated genes linked to motility, cytokine production, and angiogenesis (*Bmp2*, *Hgf*, *Il1b*, *Il6*, *Tnf*, and *Cxcl10*), while p21$^+$ VECs expressed genes important for BBB development (*Kdr*, *Cldn5*, *Icam1*, *Msfd2a*, and *Ocln*) and pericyte/macrophage recruitment (*Mcam*, *Pdgfb*, *Csf1*, *Il34*, and *S1pr1*), which is consistent with a transient pro-angiogenic state.

Receptor-ligand analysis[50] revealed reciprocal enrichment of ligands and their cognate receptors between p21$^+$ VECs and p21$^+$ brain-resident macrophages (Figure 5C; Table S4). For example, endothelial *Csf1* and *Il34* could act on macrophage *Csf1r* to promote recruitment,[51] while macrophage-secreted *Il1b* could bind endothelial *Il1r1* to stimulate migration,[52,53] thus suggesting a functional synergy. Spatially, tdT$^+$/Iba1$^+$ brain-resident macrophages were more frequently localized near tdT$^+$ vessels at E18.5 compared with tdT$^-$/Iba1$^+$ brain-resident macrophages (Figures 5D and 5F), an association that was no longer observed at PND21 (Figures 5E and 5F), which is consistent with a transient developmental interaction.

Given the role of brain-resident macrophages in angiogenic sprouts,[43,54,55] we asked whether the p21$^+$ state was enriched within vascular tip cells. p21$^+$/Cd31$^+$ cells co-expressed the tip marker Dll4 and localized near vessel sprouts (Figure 1F), where tip versus non-tip populations (39% versus 11%, respectively, $p = 1.26 \times 10^{-64}$) were enriched for p21$^+$ cells, and the transcriptional profile of tip cells correlated with p21$^+$ VECs ($p < 10^{-4}$) and overlapped with SaTS (Figure S5A; Table S3). Analysis of an independent embryonic endothelial dataset[56] confirmed the enrichment of p21$^+$ cells in tip populations across tissues (brain, 37% tip cells versus 17% non-tip cells, $p = 2.8 \times 10^{-8}$; non-brain, 12% tip cells versus 6% non-tip cells, $p = 1.9 \times 10^{-8}$), and SaTS enrichment was observed in both brain and non-brain tip populations (Figure S5A). The proportion of p21$^+$ cells was higher in brain tip cells (37% p21$^+$) than in non-brain tip cells (12% p21$^+$, $p = 2.2 \times 10^{-16}$). Together, these data support a conserved association between tip cell states and p21-associated senescent-like transcriptional programs, with enhanced representation in brain vasculature.

Embryonic p21$^+$ cells participate in brain-vasculature patterning

Given the spatiotemporal enrichment of embryonic senescent p21$^+$ cells in regions undergoing specialized barrier formation during embryogenesis, we explored the role of p21$^+$ populations in the developing vasculature and ChP. We crossed *p21-CreERT2* with a Cre-inducible diphtheria toxin A (iDTA) mouse

Please cite this article in press as: Watson et al., Persistent and transient senescent cells contribute to brain-barrier development, Cell (2026), https://doi.org/10.1016/j.cell.2026.05.022

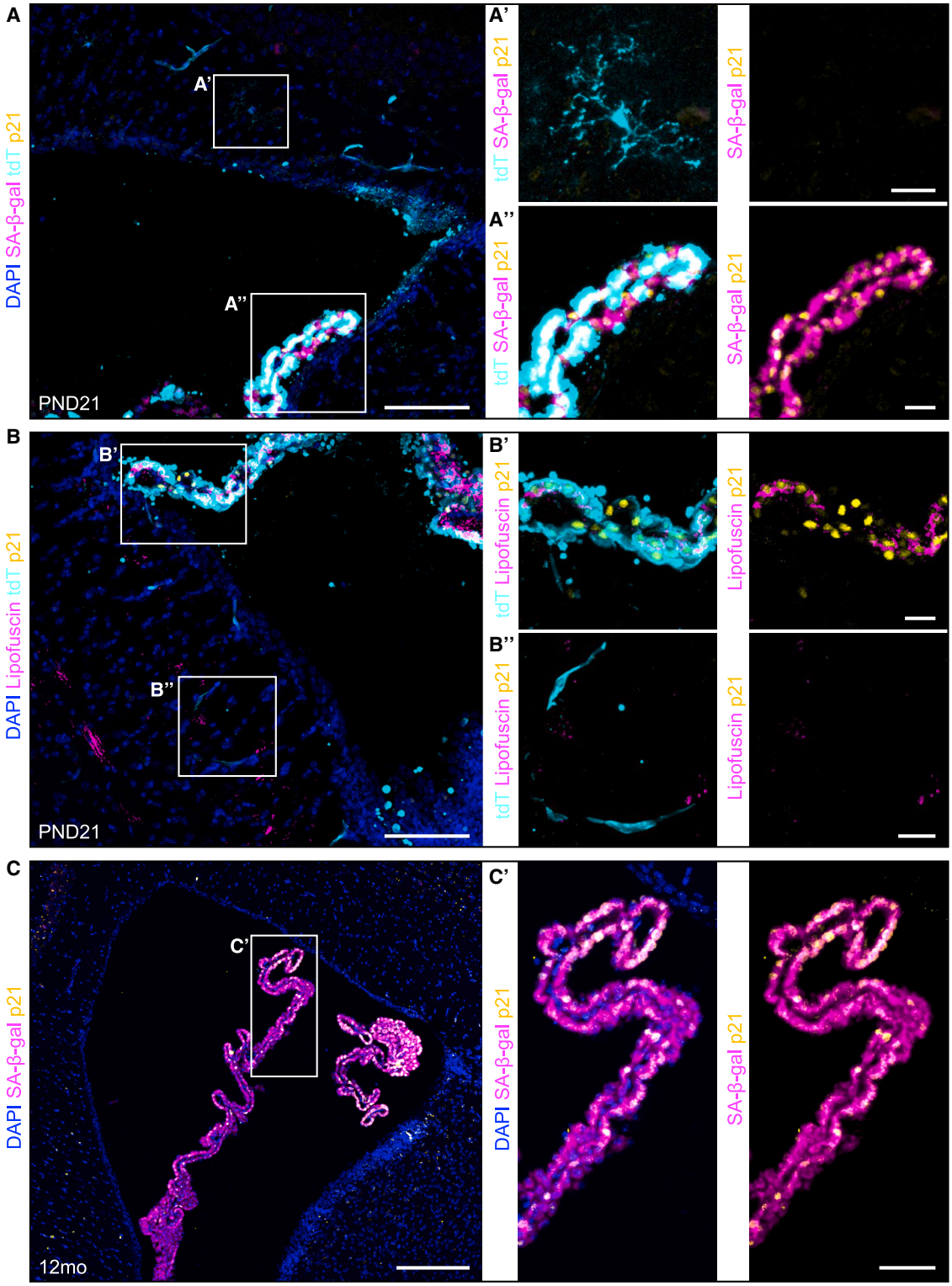


Figure 4. Embryonic p21⁺ ChPe cells retain senescence marker expression into adulthood, while senescence is transient in embryonic VECs and brain-resident Macs

(A and B) SA-β-gal (magenta; A) or lipofuscin (magenta; B), tdT (cyan), and p21 (yellow) in PND21 LV ChP after late-window tamoxifen labeling. Scale bars, 100 μm and 20 μm (A'), (A''), (B'), and (B'').

(C) SA-β-gal (magenta) and p21 (yellow) in 12-month-old LV ChP. Scale bars, 200 μm (C) and 50 μm (C').

Please cite this article in press as: Watson et al., Persistent and transient senescent cells contribute to brain-barrier development, Cell (2026), https://doi.org/10.1016/j.cell.2026.05.022

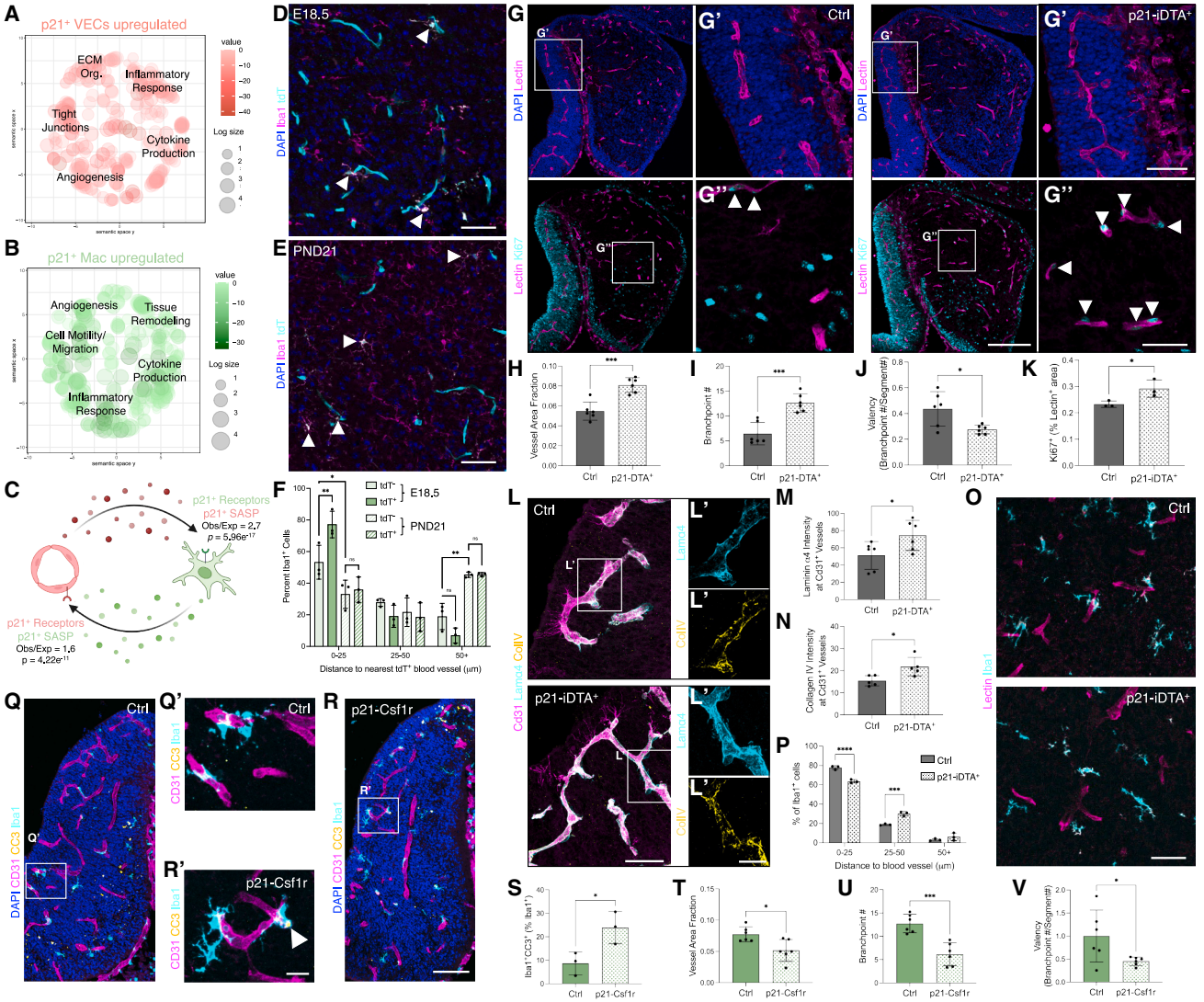


Figure 5. Embryonic p21$^+$ cell ablation disrupts brain-vasculature development

(A and B) GO analysis of upregulated genes in p21$^+$ VECs (A) and brain-resident macrophages (Mac) (B).

(C) Receptor-ligand interactions between p21$^+$ VECs and Mac.

(D–F) Mac (Iba1, magenta) and tdT (cyan) vessel proximity in the hindbrain at E18.5 (D) and PND21 (E) after late-window tamoxifen administration, n = 111–507, 3 replicates. Scale bar, 50 μm.

(G) Lectin (magenta) and Ki67 (cyan) in E15.5 midbrain-hindbrain boundary (MHB) and cerebellum. Scale bars, 200 μm and 50 μm (G') and (G'').

(H–J) Vessel area fraction (H), branchpoint # (I), and valency (J) in E15.5 MHB CD31$^+$ vasculature, n = 6.

(K) Ki67$^+$ cells (percentage lectin$^+$ area) in E15.5 cerebellum, n = 3.

(L–N) CD31 (magenta), laminin α4 (Lamα4; cyan), and collagen IV (CollV; yellow) staining and quantification in E15.5 MHB. Scale bars, 50 μm and 20 μm (L').

(O and P) Lectin (magenta) and Iba1 (cyan) staining and distance quantification in E18.5 hindbrain, n = 157–280 cells, 3 replicates. Scale bar, 50 μm.

(Q–S) CD31 (magenta), cleaved-caspase-3 (CC3; yellow), and Iba1 (cyan) staining and quantification in E16.5 MHB; n = 3. Scale bars, 100 μm and 20 μm (Q').

(T–V) Vessel area fraction (T), branchpoint # (U), and valency (V) in E16.5 CD31$^+$ vasculature, n = 6. *p < 0.05, **p < 0.01, ***p < 0.001, and ****p < 0.0001 by hypergeometric test (C), two-way ANOVA followed by Šídák's multiple comparison test (F) and (P), and unpaired two-tailed Student's t test (H)–(K), (M), (N), and (S)–(V).

See also Figures S5 and S6; Table S4.

model[57] for specific ablation of p21-expressing cells. Daily tamoxifen administration (E11.5–E15.5) caused embryonic lethality by E18.5 in Cre$^+$/DTA$^+$ (p21-iDTA$^+$) but not Cre$^-$/DTA$^+$ (control) embryos, and this was accompanied by severe developmental defects, including craniofacial anomalies, stunted growth, swelling, and hemorrhaging (Figure S5B). p21-iDTA$^+$ brains were smaller than controls (Figures S5C–S5H), with a significant reduction in p73$^+$ CR cells (Figures S5I and S5J), which confirmed the effective ablation of p21$^+$ cells with this system. Additionally, p21-iDTA$^+$ brains showed abnormal progenitor

Please cite this article in press as: Watson et al., Persistent and transient senescent cells contribute to brain-barrier development, Cell (2026), https://doi.org/10.1016/j.cell.2026.05.022

populations in the cortex (Figures S5K–S5N) and hippocampus (Figures S5O–S5Q), which is consistent with prior studies of CR cell ablation[58–60] provides a proof of principle for the efficacy of our p21-targeted ablation system.

The BBB serves as a critical interface between the vasculature and neural tissue, thus restricting the entry of blood-borne cells and solutes into the brain parenchyma.[16] Disruption of this barrier during development can lead to vascular leakage and subsequent neurodevelopmental abnormalities.[61] At E18.5, over 75% of p21-iDTA$^+$ brains had some degree of meningeal or cerebral hemorrhage (Figures S6A and S6B), and we detected the leakage of red blood cells outside vessel lumina, which is consistent with compromised vascular integrity (Figures S6C–S6E). At E15.5, p21$^+$ cell ablation led to region-specific changes in vascular patterning, which included elevated vessel coverage in the cortex, dorsal midbrain, and midbrain-hindbrain boundary (MHB), that was accompanied by increased branching and reduced vessel network complexity (valency) specifically at the MHB (Figures 5G–5J and S6F–S6H). Endothelial proliferation was increased (Figure 5K), and ECM components laminin α4 and collagen IV were elevated in the midbrain and MHB (Figures 5L–5N, S6I, and S6J), which suggests that p21$^+$ cells play a role in restraining proliferation and are associated with coordinated vascular remodeling and matrix deposition. Moreover, after the ablation of p21$^+$ cells, brain-resident macrophages were farther away from blood vessels in p21-iDTA$^+$ hindbrain relative to controls (Figures 5O and 5P), thus suggesting that p21$^+$ brain-resident macrophages preferentially associate with the developing vasculature.

To assess whether p21$^+$ brain-resident macrophages are required for proper brain vascularization, we crossed *p21-CreERT* with *Csf1r^{flox}* mice (p21-Csf1r).[62] As *Csf1r* is essential for macrophage survival,[63] its removal is anticipated to specifically deplete p21$^+$ macrophages while sparing p21$^+$ VECs, ChPe, and CR cells. Daily tamoxifen administration (E11.5–E15.5) led to increased apoptosis and a reduced number of Iba1$^+$ cells in multiple brain regions at E16.5 (Figures 5Q–5S, S6K, and S6L). Unlike p21-iDTA$^+$, no overt hemorrhage or stunted growth was observed in p21-Csf1r embryos (Figure S6M). However, we detected altered vessel patterning that was most prominent in the MHB at E16.5, which included reduced vessel density and network complexity (Figures 5Q, 5T–5V, and S6N–S6P) with no difference in basement membrane deposition (Figures S6Q–S6S).

Pan- and macrophage-specific ablation of p21$^+$ cells revealed distinct but complementary roles in regulating vascular expansion and patterning. Loss of all p21$^+$ cells resulted in increased vessel area, altered branching complexity, elevated endothelial proliferation, and enhanced basement membrane components, whereas selective depletion of p21$^+$ macrophages reduced vessel growth and branching.

Embryonic p21$^+$ cells contribute to blood-CSF barrier development and function

ChPe cells are specialized secretory epithelial cells with abundant apical microvilli and cilia that contribute to CSF sensing and homeostasis.[20,64] They regulate CSF composition through ion channels and transporters at the blood-CSF interface.[23,65,66] Genes upregulated in both SaTS and p21$^+$ ChPe cells were enriched for processes supporting these functions, including ciliogenesis, ion transport, and cell adhesion (Figures 6A, S3E, and S7A), which indicated that senescence-associated gene expression aligns with epithelial barrier function and fluid regulation. Upregulated genes were involved in cilium assembly and ventricular flow (*Rsph9*, *Dnah2*, *Ulk4*, *Kif3a*, and *Ccdc39*),[67–70] adhesion and polarity (*Ocln*, *Cldn1/2/3*, *Plxnb2*, and *Tjp2/3*),[71] and epithelial-endothelial signaling (*Vegfa/b*, *Pdgfa*, and *Angptl2*),[21,72] as well as anti-apoptotic, metabolic, and transport-related genes (*Bcl2l1*, *Bcl6*, *Lpin1*, *Pld1, Slc22a17*, and *Slc1a2*). Together, these observations indicate that p21$^+$ ChPe cells engage senescence-associated features that support epithelial function in non-regenerating tissues.

To assess the functional contribution of p21$^+$ ChPe cells, we ablated p21$^+$ populations between E11.5–E15.5 using the p21-iDTA$^+$ system. This resulted in edema and fluid accumulation around the head and neck regions by E15.5 (Figures 6B and S7B). At E18.5, ChP size was reduced in both the LV (∼44%) and 4V (∼42%), accompanied by reduced ventricular area (∼41%; Figures 6C–6E, S7C, and S7D). Magnetic resonance imaging (MRI) analysis revealed reduced ventricular fluid (∼45% in LV and ∼30% in 4V; Figures 6F and 6G) and increased extracranial fluid accumulation (Figures 6F, 6H, S7E, and S7F), thus indicating disrupted fluid homeostasis that likely reflects both impaired CSF regulation and systemic effects of widespread p21$^+$ cell ablation. Since CSF production requires vascular delivery of plasma-derived solutes and their active transport through ChPe water and ion channels,[73] we examined these components following ablation. Expression of Aqp1, a water channel essential for CSF secretion, was reduced in the LV ChP of p21-iDTA$^+$ embryos at E18.5 (Figures 6I and 6J). Additionally, we observed a significant reduction in Cd31$^+$ endothelial cells in the LV ChP (Figures 6I and 6K), which is consistent with a compromised vascular supply. Notably, collagen IV intensity was also reduced in the ChP (Figures 6L and 6M), which is indicative of an impaired ECM integrity that is contributing to barrier dysfunction.

Barrier integrity at the blood-CSF interface depends on epithelial polarity, adhesion, and ECM interactions.[20] Correspondingly, senescence-associated adhesion and polarity-associated genes were enriched in p21$^+$ ChPe cells (Figure 6A; Table S3). Following ablation, plexin B2 (Plxnb2) and integrin β1 were reduced (Figures 6L, 6N, and S7G), and ZO-1/F-actin organization was altered (Figure S7H). Increased erythrocyte accumulation in the ventricle (Figures S7I and S7J) further indicated compromised barrier integrity. Together, these findings indicate that p21$^+$ cells support epithelial organization and blood-CSF barrier function.

DISCUSSION

Embryonic senescence and brain-barrier development

Our findings reveal p21$^+$ populations across ChPe cells, VECs, and brain-resident macrophages that exhibit features of cellular senescence during brain-barrier formation, with lineage-specific implementations that address the distinct physiological demands of the BBB and blood-CSF barrier. ChPe cells maintain a persistent non-inflammatory state associated with barrier

Please cite this article in press as: Watson et al., Persistent and transient senescent cells contribute to brain-barrier development, Cell (2026), https://doi.org/10.1016/j.cell.2026.05.022

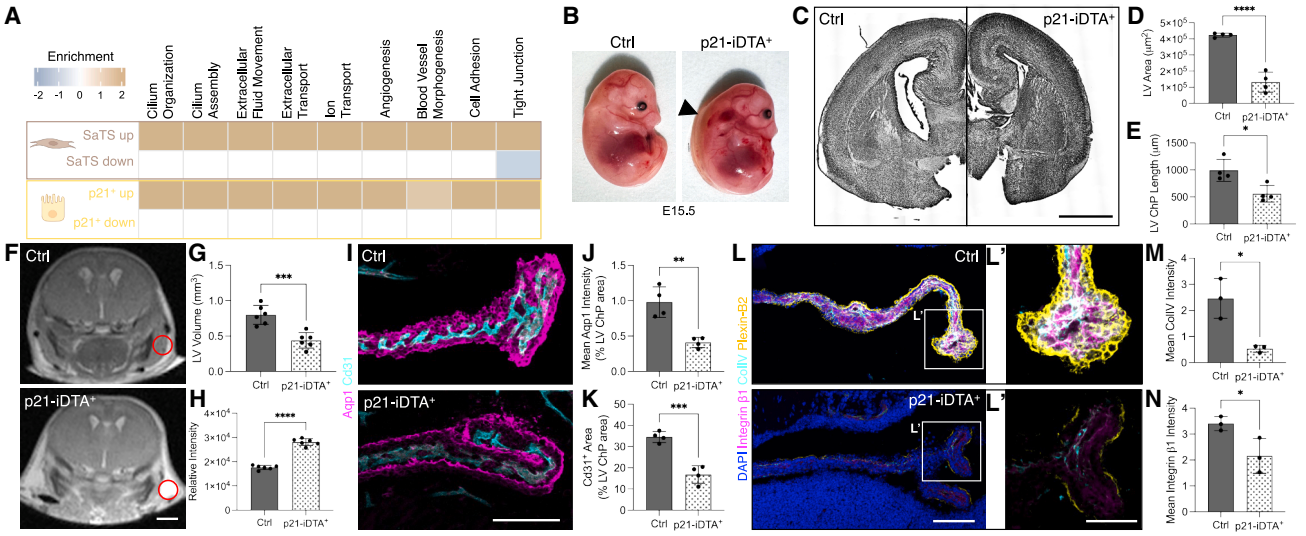


Figure 6. Embryonic p21$^+$ cell ablation results in aberrant blood-CSF barrier formation and function

(A) GO enrichment of SaTS and shared genes in p21$^+$ ChPe cells.

(B) Control and p21-iDTA$^+$ embryos at E15.5. Arrowhead indicates fluid accumulation under the skin.

(C) Nissl-stained E18.5 forebrain. Scale bar, 1 mm.

(D and E) LV ChP area (μm^2; D) and length (μm; E), $n = 4$.

(F–H) MRI representative images and analysis. Representative region of interest (ROI) used for signal intensity measurements (H) is indicated with red circles. Scale bar, 1 mm.

(G) LV volume (mm^3) from control and p21-iDTA$^+$ MRI, $n = 6$.

(H) MR signal intensity in identical control and p21-iDTA$^+$ ROI, $n = 6$.

(I) Aqp1 (magenta) and CD31 (cyan) in E18.5 LV ChP. Scale bar: 50 μm.

(J and K) Aqp1 intensity (J) and CD31 area (K) per LV ChP, $n = 4$.

(L–N) Plexin-B2 (yellow), CollV (cyan), and integrin β1 (magenta) staining and quantification in E18.5 control and p21-iDTA$^+$ LV ChP, $n = 3$–4. Scale bars, 100 μm and 50 μm (L′). *$p < 0.05$, **$p < 0.01$, ***$p < 0.001$, and ****$p < 0.0001$ by unpaired two-tailed Student's t test.

See also Figure S7.

support, whereas VECs and brain-resident macrophages transiently adopt pro-inflammatory senescence states linked to paracrine signaling and tissue remodeling. Accordingly, the ablation of all p21$^+$ cells resulted in severe structural and functional defects, including cerebral hemorrhage, ventricular collapse, and abnormal vascular patterning, which underscores the importance of p21$^+$ populations for brain-barrier integrity. These findings support a model in which senescence is not a binary cell fate, but a modular program whose features are selectively deployed in a context-dependent manner to influence tissue development and barrier formation.

Endothelial tip cells are enriched for p21 expression and display transcriptional features overlapping with senescence programs, which is consistent with a senescence-like angiogenic state associated with restrained proliferation and coordinated sprouting. In parallel, p21$^+$ macrophages localize near p21$^+$ endothelial cells and upregulate angiocrine and matrix-remodeling factors. Selective ablation of p21$^+$ macrophages reduced vessel density and branching complexity, in contrast to the hypervascular phenotype observed following pan-p21$^+$ cell ablation. These outcomes indicate complementary roles for distinct p21$^+$ populations: p21$^+$ endothelial cells are associated with sprouting behavior and features of vessel maturation, whereas p21$^+$ macrophages provide local patterning and remodeling cues, potentially through SASP-associated factors.[74–77] Notably, the transient nature of tip cells, together with similar states in macrophages, supports context-dependent and reversible engagement of senescence-associated features that are integrated with angiogenic and remodeling processes, rather than representing a fixed terminal state.

Lifelong ChP senescence: Redefining a physiological state

The persistence of senescent ChPe cells into late adulthood challenges the prevailing binary view of senescence as either transient and beneficial during development or chronic and deleterious in adult tissues.[1,2,5] Unlike classical senescence, which is typically associated with chronic SASP-driven inflammation and tissue degeneration, ChPe cells appear to refine the secretory phenotype into a stable, non-inflammatory state that supports long-term physiological function. By entering a senescent state early in development, ChPe cells may acquire defining attributes suited to the demands of the brain-CSF interface, which include stable cell-cycle exit in a largely non-regenerative niche, reinforcement of barrier integrity through enhanced ECM, dynamic cilium organization, trophic signaling, and solute transport. These features suggest a solution to a fundamental biological challenge: how a post-mitotic, highly secretory epithelium maintains functional stability over decades in the absence of cellular

Please cite this article in press as: Watson et al., Persistent and transient senescent cells contribute to brain-barrier development, Cell (2026), https://doi.org/10.1016/j.cell.2026.05.022

turnover. While transient developmental senescence has been described in multiple embryonic contexts,[3,4] no somatic cell population has previously been shown to retain senescence as a lifelong physiological state. The persistence of senescence markers without inflammatory or degenerative signatures indicates that ChPe cells maintain a regulated, beneficial senescent state. Understanding how this is achieved may hold clues for targeting senescence in disease contexts where secretory profiles become maladaptive.

Reconciling senescence in development and aging

Our findings support a framework reconciling the duality of senescence in development and aging.[5] Rather than arising as a distinct pathological state in aged tissues, many of the defining features of cellular senescence appear to derive from mechanisms originally used during embryogenesis to coordinate tissue patterning, barrier formation, and long-term structural stability. In aging, senescent cells accumulate across numerous populations in the brain, including microglia, astrocytes, oligodendrocytes, endothelial cells, and ChPe cells, where they contribute to neuroinflammation, barrier dysfunction, and cognitive decline.[9,10,78–81] In neurodegenerative disorders, the clearance of senescent cells improves cognitive function and reduces neuropathology,[9,80,81] which reinforces the view that senescence contributes to age-related brain dysfunction. Simultaneously, core features of senescence, including SASP-driven signaling and ECM remodeling, can serve constructive functions. *In vitro* senescence models consistently upregulate barrier-associated pathways, including ECM components, junctional proteins (claudins, occludin, and ZO-1), transporters, and ciliary factors. During development, these features are deployed in a controlled, time-limited manner within distinct cell types. This convergence suggests that barrier-associated functions are a prominent feature of senescence-associated transcriptional programs, with regulated deployment contributing to brain-barrier formation.

Clearance of senescent cells improves outcomes in aging and neurodegenerative models,[9,10,80,81] yet the removal of senescent epithelial cells can impair barrier integrity and promote pathology.[82] Taken together with our findings, these observations suggest that therapeutic targeting of senescent cells may require careful consideration of lineage-specific functions and the contexts in which these cells persist. In this framework, senescence is a context-dependent process that supports development and homeostasis when appropriately regulated but becomes detrimental when chronically engaged or unresolved. Defining lineage-specific senescence programs, such as the apparent uncoupling of inflammatory SASP factors from barrier-supportive secretory functions in ChPe cells, may therefore enable more precise therapeutic strategies.

Limitations of the study

This study relies on p21 expression to identify and genetically ablate senescent cells during embryonic development. While p21 is a well-established marker of senescence in developmental contexts,[3,4] its expression is not exclusive to senescent cells; therefore, pan-ablation of p21$^+$ cells may introduce off-target effects unrelated to senescence. In addition, the p21-driven ablation strategy eliminates entire cells rather than selectively perturbing senescence-associated molecular programs, which limits our ability to distinguish whether the observed phenotypes arise from the senescence program itself or from the loss of other essential cellular functions. Additionally, the pan-p21$^+$ cell ablation approach lacks cell-type specificity, which results in the simultaneous ablation of multiple p21$^+$ populations, including VECs, ChPe cells, macrophages, and CR cells, as well as p21$^+$ cells outside the brain. Consequently, developmental phenotypes of pan-p21$^+$ cell ablation such as hemorrhage, barrier disruption, and vascular-patterning defects cannot be definitively attributed to any single population and may include indirect systemic effects. Finally, as all experiments were performed in mice, species-specific differences may influence the extent to which these findings generalize to human brain development and disease.

RESOURCE AVAILABILITY

Lead contact

Further information and requests for resources and reagents should be directed to and will be fulfilled by the lead contact, Hiruy S. Meharena (hmeharena@ucsd.edu).

Materials availability

- The mouse lines generated in this study are available upon request.

Data and code availability

- This paper analyzes existing, publicly available data, which is accessible at GEO: GSE117278, GSE202032, and GSE216970 and SRA: PRJNA637987.
- This paper does not report any original code.
- Any additional information required to reanalyze the data reported in this paper is available from the lead contact upon request.

ACKNOWLEDGMENTS

This work was supported by grants from the National Institute of Health (1R01HD115635-01, received by H.S.M.) and startup funds provided to H.S.M. by the University of California, San Diego, Departments of Neurobiology and Molecular Biology. The MRI aspects of this study were partially supported by the NIH grant S10-OD032343-01 (D.B.B.). We would like to thank the Washington University Genome Engineering and Stem Cell Center for the design of the sgRNAs and the donor construct used to generate the *p21-CreERT2* transgenic mouse line. We would also like to thank the University of California, San Diego, transgenic mouse shared resource (supported by NIH P30 CA023100 and NIH P30 DK063491) for the injection of the Cas9 protein mixed with targeting sgRNA and donor construct into pronuclear stage embryos (C57BL/6NHsd) that were implanted into foster female mice. We also wish to thank Dr. N.G. Bérubé and Dr. C.M. Noviello and all members of the Meharena lab for their constructive discussions and feedback on the manuscript. Schematic images were created using BioRender.com.

AUTHOR CONTRIBUTIONS

Conceptualization, L.A.W. and H.S.M.; methodology, L.A.W., Z.A., G.T.C., D.B.B., Z.Z., and H.S.M.; investigation, L.A.W., Z.A., M.J.C., G.T.C., K.L.J.-R., H.D., D.B.B., Z.Z., M.C.P., R.H.P., J.M.A., and H.S.M.; writing—original draft, L.A.W. and H.S.M.; writing—review & editing, L.A.W., Z.A., and H.S.M.; funding acquisition, H.S.M.; resources, H.S.M.; supervision, L.A.W. and H.S.M.

DECLARATION OF INTERESTS

The authors declare no competing interests.

DECLARATION OF GENERATIVE AI AND AI-ASSISTED TECHNOLOGIES IN THE WRITING PROCESS

During the preparation of this work, the authors used ChatGPT to check for grammar and style. After using this tool or service, the authors reviewed and edited the content as needed and take full responsibility for the content of the publication.

STAR★METHODS

Detailed methods are provided in the online version of this paper and include the following:

- KEY RESOURCES TABLE
- EXPERIMENTAL MODEL AND STUDY PARTICIPANT DETAILS
  - Mice
- METHOD DETAILS
  - Tissue collection and processing for immunostaining and histology
  - Immunostaining and histology
  - Confocal imaging and analysis
  - p21 and SA-β-gal quantification
  - tdTomato quantification
  - Vascular cells
  - Macrophage cells
  - Choroid Plexus
  - CR cells
  - Quantification in $p21^+$ and $p21^-$ cells
  - Ki67 quantification of tdT^+ and tdT^- cells
  - Blood vessel morphology analysis
  - Laminin α4, and Collagen IV intensity in $Cd31^+$ blood vessels
  - Cresyl violet quantifications
  - Signal intensity (Aqp1, Plxnb2, Integrin β1) and Cd31 area in the ChP
  - Bulk and single-cell RNA-sequencing analysis
- QUANTIFICATION AND STATISTICAL ANALYSIS
  - Permutation tests
  - Correlation analysis

SUPPLEMENTAL INFORMATION

Supplemental information can be found online at https://doi.org/10.1016/j.cell.2026.05.022.

Received: July 3, 2025
Revised: January 1, 2026
Accepted: May 15, 2026

REFERENCES

1. Rhinn, M., Ritschka, B., and Keyes, W.M. (2019). Cellular senescence in development, regeneration and disease. Development *146*, dev151837. https://doi.org/10.1242/dev.151837.
2. Huang, W., Hickson, L.J., Eirin, A., Kirkland, J.L., and Lerman, L.O. (2022). Cellular senescence: the good, the bad and the unknown. Nat. Rev. Nephrol. *18*, 611–627. https://doi.org/10.1038/s41581-022-00601-z.
3. Storer, M., Mas, A., Robert-Moreno, A., Pecoraro, M., Ortells, M.C., Di Giacomo, V., Yosef, R., Pilpel, N., Krizhanovsky, V., Sharpe, J., et al. (2013). Senescence is a developmental mechanism that contributes to embryonic growth and patterning. Cell *155*, 1119–1130. https://doi.org/10.1016/j.cell.2013.10.041.
4. Muñoz-Espín, D., Cañamero, M., Maraver, A., Gómez-López, G., Contreras, J., Murillo-Cuesta, S., Rodríguez-Baeza, A., Varela-Nieto, I., Ruberte, J., Collado, M., et al. (2013). Programmed cell senescence during mammalian embryonic development. Cell *155*, 1104–1118. https://doi.org/10.1016/j.cell.2013.10.019.
5. de Magalhães, J.P. (2024). Cellular senescence in normal physiology. Science *384*, 1300–1301. https://doi.org/10.1126/science.adj7050.
6. Gal, H., Lysenko, M., Stroganov, S., Vadai, E., Youssef, S.A., Tzadikevitch-Geffen, K., Rotkopf, R., Biron-Shental, T., de Bruin, A., Neeman, M., et al. (2019). Molecular pathways of senescence regulate placental structure and function. EMBO J. *38*, e100849. https://doi.org/10.15252/embj.2018100849.
7. Coppé, J.-P., Desprez, P.-Y., Krtolica, A., and Campisi, J. (2010). The Senescence-Associated Secretory Phenotype: The Dark Side of Tumor Suppression. Annu. Rev. Pathol. Mech. Dis. *5*, 99–118. https://doi.org/10.1146/annurev-pathol-121808-102144.
8. Mavrogonatou, E., Pratsinis, H., Papadopoulou, A., Karamanos, N.K., and Kletsas, D. (2019). Extracellular matrix alterations in senescent cells and their significance in tissue homeostasis. Matrix Biol. *75–76*, 27–42. https://doi.org/10.1016/j.matbio.2017.10.004.
9. Bussian, T.J., Aziz, A., Meyer, C.F., Swenson, B.L., van Deursen, J.M., and Baker, D.J. (2018). Clearance of senescent glial cells prevents tau-dependent pathology and cognitive decline. Nature *562*, 578–582. https://doi.org/10.1038/s41586-018-0543-y.
10. Ogrodnik, M., Evans, S.A., Fielder, E., Victorelli, S., Kruger, P., Salmonowicz, H., Weigand, B.M., Patel, A.D., Pirtskhalava, T., Inman, C.L., et al. (2021). Whole-body senescent cell clearance alleviates age-related brain inflammation and cognitive impairment in mice. Aging Cell *20*, e13296. https://doi.org/10.1111/acel.13296.
11. Rhinn, M., Zapata-Bodalo, I., Klein, A., Plassat, J.-L., Knauer-Meyer, T., and Keyes, W.M. (2022). Aberrant induction of p19Arf-mediated cellular senescence contributes to neurodevelopmental defects. PLOS Biol. *20*, e3001664. https://doi.org/10.1371/journal.pbio.3001664.
12. Meharena, H.S., Marco, A., Dileep, V., Lockshin, E.R., Akatsu, G.Y., Mullahoo, J., Watson, L.A., Ko, T., Guerin, L.N., Abdurrob, F., et al. (2022). Down-syndrome-induced senescence disrupts the nuclear architecture of neural progenitors. Cell Stem Cell *29*, 116–130.e7. https://doi.org/10.1016/j.stem.2021.12.002.
13. Xu, C., Shen, W.-B., Reece, E.A., Hasuwa, H., Harman, C., Kaushal, S., and Yang, P. (2021). Maternal diabetes induces senescence and neural tube defects sensitive to the senomorphic rapamycin. Sci. Adv. *7*, eabf5089. https://doi.org/10.1126/sciadv.abf5089.
14. Kintner, C. (2002). Neurogenesis in Embryos and in Adult Neural Stem Cells. J. Neurosci. *22*, 639–643. https://doi.org/10.1523/JNEUROSCI.22-03-00639.2002.
15. Lehtinen, M.K., and Walsh, C.A. (2011). Neurogenesis at the brain-cerebrospinal fluid interface. Annu. Rev. Cell Dev. Biol. *27*, 653–679. https://doi.org/10.1146/annurev-cellbio-092910-154026.
16. Daneman, R., and Prat, A. (2015). The Blood–Brain Barrier. Cold Spring Harb. Perspect. Biol. *7*, a020412. https://doi.org/10.1101/cshperspect.a020412.
17. Denes, A., Hansen, C.E., Oezorhan, U., Figuerola, S., de Vries, H.E., Sorokin, L., Planas, A.M., Engelhardt, B., and Schwaninger, M. (2024). Endothelial cells and macrophages as allies in the healthy and diseased brain. Acta Neuropathol. *147*, 38. https://doi.org/10.1007/s00401-024-02695-0.
18. Lindahl, P., Johansson, B.R., Levéen, P., and Betsholtz, C. (1997). Pericyte loss and microaneurysm formation in PDGF-B-deficient mice. Science *277*, 242–245. https://doi.org/10.1126/science.277.5323.242.
19. Saunders, N.R., Dziegielewska, K.M., Fame, R.M., Lehtinen, M.K., and Liddelow, S.A. (2023). The choroid plexus: a missing link in our understanding of brain development and function. Physiol. Rev. *103*, 919–956. https://doi.org/10.1152/physrev.00060.2021.
20. Lun, M.P., Monuki, E.S., and Lehtinen, M.K. (2015). Development and functions of the choroid plexus–cerebrospinal fluid system. Nat. Rev. Neurosci. *16*, 445–457. https://doi.org/10.1038/nrn3921.

Please cite this article in press as: Watson et al., Persistent and transient senescent cells contribute to brain-barrier development, Cell (2026), https://doi.org/10.1016/j.cell.2026.05.022

21. Kompaníková, P., and Bryja, V. (2022). Regulation of choroid plexus development and its functions. Cell. Mol. Life Sci. *79*, 304. https://doi.org/10.1007/s00018-022-04314-1.

22. McDonald, T.F., and Green, K. (1988). Cell turnover in ciliary epithelium compared to other slow renewing epithelia in the adult mouse. Curr. Eye Res. *7*, 247–252. https://doi.org/10.3109/02713688809047029.

23. Lehtinen, M.K., Zappaterra, M.W., Chen, X., Yang, Y.J., Hill, A.D., Lun, M., Maynard, T., Gonzalez, D., Kim, S., Ye, P., et al. (2011). The cerebrospinal fluid provides a proliferative niche for neural progenitor cells. Neuron *69*, 893–905. https://doi.org/10.1016/j.neuron.2011.01.023.

24. Dani, N., Herbst, R.H., McCabe, C., Green, G.S., Kaiser, K., Head, J.P., Cui, J., Shipley, F.B., Jang, A., Dionne, D., et al. (2021). A cellular and spatial map of the choroid plexus across brain ventricles and ages. Cell *184*, 3056–3074.e21. https://doi.org/10.1016/j.cell.2021.04.003.

25. La Manno, G., Siletti, K., Furlan, A., Gyllborg, D., Vinsland, E., Mossi Albiach, A., Mattsson Langseth, C., Khven, I., Lederer, A.R., Dratva, L.M., et al. (2021). Molecular architecture of the developing mouse brain. Nature *596*, 92–96. https://doi.org/10.1038/s41586-021-03775-x.

26. Gorgoulis, V., Adams, P.D., Alimonti, A., Bennett, D.C., Bischof, O., Bishop, C., Campisi, J., Collado, M., Evangelou, K., Ferbeyre, G., et al. (2019). Cellular Senescence: Defining a Path Forward. Cell *179*, 813–827. https://doi.org/10.1016/j.cell.2019.10.005.

27. Yan, J., Chen, S., Yi, Z., Zhao, R., Zhu, J., Ding, S., and Wu, J. (2024). The role of p21 in cellular senescence and aging-related diseases. Mol. Cells *47*, 100113. https://doi.org/10.1016/j.mocell.2024.100113.

28. Siegenthaler, J.A., and Miller, M.W. (2005). Transforming growth factor beta 1 promotes cell cycle exit through the cyclin-dependent kinase inhibitor p21 in the developing cerebral cortex. J. Neurosci. *25*, 8627–8636. https://doi.org/10.1523/JNEUROSCI.1876-05.2005.

29. Karimian, A., Ahmadi, Y., and Yousefi, B. (2016). Multiple functions of p21 in cell cycle, apoptosis and transcriptional regulation after DNA damage. DNA Repair *42*, 63–71. https://doi.org/10.1016/j.dnarep.2016.04.008.

30. Ogrodnik, M., Carlos Acosta, J., Adams, P.D., d'Adda di Fagagna, F., Baker, D.J., Bishop, C.L., Chandra, T., Collado, M., Gil, J., Gorgoulis, V., et al. (2024). Guidelines for minimal information on cellular senescence experimentation in vivo. Cell *187*, 4150–4175. https://doi.org/10.1016/j.cell.2024.05.059.

31. Suryadevara, V., Hudgins, A.D., Rajesh, A., Pappalardo, A., Karpova, A., Dey, A.K., Hertzel, A., Agudelo, A., Rocha, A., Soygur, B., et al. (2024). SenNet recommendations for detecting senescent cells in different tissues. Nat. Rev. Mol. Cell Biol. *25*, 1001–1023. https://doi.org/10.1038/s41580-024-00738-8.

32. Sturmlechner, I., Zhang, C., Sine, C.C., van Deursen, E.-J., Jeganathan, K.B., Hamada, N., Grasic, J., Friedman, D., Stutchman, J.T., Can, I., et al. (2021). p21 produces a bioactive secretome that places stressed cells under immunosurveillance. Science *374*, eabb3420. https://doi.org/10.1126/science.abb3420.

33. Marin, I., Boix, O., Garcia-Garijo, A., Sirois, I., Caballe, A., Zarzuela, E., Ruano, I., Attolini, C.S.-O., Prats, N., López-Domínguez, J.A., et al. (2023). Cellular Senescence Is Immunogenic and Promotes Antitumor Immunity. Cancer Discov. *13*, 410–431. https://doi.org/10.1158/2159-8290.CD-22-0523.

34. Saul, D., Kosinsky, R.L., Atkinson, E.J., Doolittle, M.L., Zhang, X., LeBrasseur, N.K., Pignolo, R.J., Robbins, P.D., Niedernhofer, L.J., Ikeno, Y., et al. (2022). A new gene set identifies senescent cells and predicts senescence-associated pathways across tissues. Nat. Commun. *13*, 4827. https://doi.org/10.1038/s41467-022-32552-1.

35. Chatsirisupachai, K., Palmer, D., Ferreira, S., and de Magalhães, J.P. (2019). A human tissue-specific transcriptomic analysis reveals a complex relationship between aging, cancer, and cellular senescence. Aging Cell *18*, e13041. https://doi.org/10.1111/acel.13041.

36. Lee, B.Y., Han, J.A., Im, J.S., Morrone, A., Johung, K., Goodwin, E.C., Kleijer, W.J., DiMaio, D., and Hwang, E.S. (2006). Senescence-associated beta-galactosidase is lysosomal beta-galactosidase. Aging Cell *5*, 187–195. https://doi.org/10.1111/j.1474-9726.2006.00199.x.

37. Davan-Wetton, C.S.A., and Montero-Melendez, T. (2024). An optimised protocol for the detection of lipofuscin, a versatile and quantifiable marker of cellular senescence. PLOS One *19*, e0306275. https://doi.org/10.1371/journal.pone.0306275.

38. Uhlén, M., Fagerberg, L., Hallström, B.M., Lindskog, C., Oksvold, P., Mardinoglu, A., Sivertsson, Å., Kampf, C., Sjöstedt, E., Asplund, A., et al. (2015). Tissue-based map of the human proteome. Science *347*, 1260419. https://doi.org/10.1126/science.1260419.

39. Lun, M.P., Johnson, M.B., Broadbelt, K.G., Watanabe, M., Kang, Y.-J., Chau, K.F., Springel, M.W., Malesz, A., Sousa, A.M.M., Pletikos, M., et al. (2015). Spatially heterogeneous choroid plexus transcriptomes encode positional identity and contribute to regional CSF production. J. Neurosci. *35*, 4903–4916. https://doi.org/10.1523/JNEUROSCI.3081-14.2015.

40. Madisen, L., Zwingman, T.A., Sunkin, S.M., Oh, S.W., Zariwala, H.A., Gu, H., Ng, L.L., Palmiter, R.D., Hawrylycz, M.J., Jones, A.R., et al. (2010). A robust and high-throughput Cre reporting and characterization system for the whole mouse brain. Nat. Neurosci. *13*, 133–140. https://doi.org/10.1038/nn.2467.

41. Elorriaga, V., Pierani, A., and Causeret, F. (2023). Cajal-retzius cells: Recent advances in identity and function. Curr. Opin. Neurobiol. *79*, 102686. https://doi.org/10.1016/j.conb.2023.102686.

42. Causeret, F., Coppola, E., and Pierani, A. (2018). Cortical developmental death: selected to survive or fated to die. Curr. Opin. Neurobiol. *53*, 35–42. https://doi.org/10.1016/j.conb.2018.04.022.

43. Fantin, A., Vieira, J.M., Gestri, G., Denti, L., Schwarz, Q., Prykhozhij, S., Peri, F., Wilson, S.W., and Ruhrberg, C. (2010). Tissue macrophages act as cellular chaperones for vascular anastomosis downstream of VEGF-mediated endothelial tip cell induction. Blood *116*, 829–840. https://doi.org/10.1182/blood-2009-12-257832.

44. Fantin, A., Vieira, J.M., Plein, A., Maden, C.H., and Ruhrberg, C. (2013). The embryonic mouse hindbrain as a qualitative and quantitative model to study the molecular and cellular mechanisms of angiogenesis. Nat. Protoc. *8*, 418–429. https://doi.org/10.1038/nprot.2013.015.

45. Tam, S.J., and Watts, R.J. (2010). Connecting Vascular and Nervous System Development: Angiogenesis and the Blood-Brain Barrier. Annu. Rev. Neurosci. *33*, 379–408. https://doi.org/10.1146/annurev-neuro-060909-152829.

46. Ben-Zvi, A., Lacoste, B., Kur, E., Andreone, B.J., Mayshar, Y., Yan, H., and Gu, C. (2014). Mfsd2a is critical for the formation and function of the blood-brain barrier. Nature *509*, 507–511. https://doi.org/10.1038/nature13324.

47. Courtney, Y., Head, J.P., Dani, N., Chechneva, O.B., Shipley, F.B., Zhang, Y., Moltzman, M.J., Sadegh, C., Libermann, T.A., and Lehtinen, M.K. (2025). A choroid plexus apocrine secretion mechanism shapes CSF proteome and embryonic brain development. Nat. Neurosci. *28*, 1446–1459. https://doi.org/10.1038/s41593-025-01972-9.

48. Hogan, K.A., and Bautch, V.L. (2004). Blood vessel patterning at the embryonic midline. Curr. Top. Dev. Biol. *62*, 55–85. https://doi.org/10.1016/S0070-2153(04)62003-5.

49. Li, Y., Zhao, H., Huang, X., Tang, J., Zhang, S., Li, Y., Liu, X., He, L., Ju, Z., Lui, K.O., et al. (2018). Embryonic senescent cells re-enter cell cycle and contribute to tissues after birth. Cell Res. *28*, 775–778. https://doi.org/10.1038/s41422-018-0050-6.

50. Armingol, E., Officer, A., Harismendy, O., and Lewis, N.E. (2021). Deciphering cell–cell interactions and communication from gene expression. Nat. Rev. Genet. *22*, 71–88. https://doi.org/10.1038/s41576-020-00292-x.

51. Goldmann, T., Wieghofer, P., Jordão, M.J.C., Prutek, F., Hagemeyer, N., Frenzel, K., Amann, L., Staszewski, O., Kierdorf, K., Krueger, M., et al. (2016). Origin, fate and dynamics of macrophages at CNS interfaces. Nat. Immunol. *17*, 797–805. https://doi.org/10.1038/ni.3423.

Please cite this article in press as: Watson et al., Persistent and transient senescent cells contribute to brain-barrier development, Cell (2026), https://doi.org/10.1016/j.cell.2026.05.022

52. Fahey, E., and Doyle, S.L. (2019). IL-1 Family Cytokine Regulation of Vascular Permeability and Angiogenesis. Front. Immunol. *10*, 1426. https://doi.org/10.3389/fimmu.2019.01426.

53. Voronov, E., Carmi, Y., and Apte, R.N. (2014). The role IL-1 in tumor-mediated angiogenesis. Front. Physiol. *5*, 114. https://doi.org/10.3389/fphys.2014.00114.

54. Shah, F.H., and Lee, H.-W. (2024). Endothelial and macrophage interactions in the angiogenic niche. Cytokine Growth Factor Rev. *78*, 64–76. https://doi.org/10.1016/j.cytogfr.2024.07.005.

55. Zajac, E., Schweighofer, B., Kupriyanova, T.A., Juncker-Jensen, A., Minder, P., Quigley, J.P., and Deryugina, E.I. (2013). Angiogenic capacity of M1- and M2-polarized macrophages is determined by the levels of TIMP-1 complexed with their secreted proMMP-9. Blood *122*, 4054–4067. https://doi.org/10.1182/blood-2013-05-501494.

56. Chen, J., Zhang, X., DeLaughter, D.M., Trembley, M.A., Saifee, S., Xiao, F., Chen, J., Zhou, P., Seidman, C.E., Seidman, J.G., et al. (2024). Molecular and Spatial Signatures of Mouse Embryonic Endothelial Cells at Single-Cell Resolution. Circ. Res. *134*, 529–546. https://doi.org/10.1161/CIRCRESAHA.123.323956.

57. Voehringer, D., Liang, H.-E., and Locksley, R.M. (2008). Homeostasis and effector function of lymphopenia-induced "memory-like" T cells in constitutively T cell-depleted mice. J. Immunol. *180*, 4742–4753. https://doi.org/10.4049/jimmunol.180.7.4742.

58. Hodge, R.D., Garcia, A.J., Elsen, G.E., Nelson, B.R., Mussar, K.E., Reiner, S.L., Ramirez, J.-M., and Hevner, R.F. (2013). Tbr2 Expression in Cajal-Retzius Cells and Intermediate Neuronal Progenitors Is Required for Morphogenesis of the Dentate Gyrus. J. Neurosci. *33*, 4165–4180. https://doi.org/10.1523/JNEUROSCI.4185-12.2013.

59. Talos, F., Abraham, A., Vaseva, A.V., Holembowski, L., Tsirka, S.E., Scheel, A., Bode, D., Dobbelstein, M., Brück, W., and Moll, U.M. (2010). p73 is an essential regulator of neural stem cell maintenance in embryonal and adult CNS neurogenesis. Cell Death Differ. *17*, 1816–1829. https://doi.org/10.1038/cdd.2010.131.

60. Soriano, E., Alvarado-Mallart, R.M., Dumesnil, N., Del Río, J.A., and Sotelo, C. (1997). Cajal-Retzius Cells Regulate the Radial Glia Phenotype in the Adult and Developing Cerebellum and Alter Granule Cell Migration. Neuron *18*, 563–577. https://doi.org/10.1016/S0896-6273(00)80298-6.

61. Obermeier, B., Daneman, R., and Ransohoff, R.M. (2013). Development, maintenance and disruption of the blood-brain barrier. Nat. Med. *19*, 1584–1596. https://doi.org/10.1038/nm.3407.

62. Li, J., Chen, K., Zhu, L., and Pollard, J.W. (2006). Conditional deletion of the colony stimulating factor-1 receptor (c-fms proto-oncogene) in mice. Genesis *44*, 328–335. https://doi.org/10.1002/dvg.20219.

63. Dai, X.-M., Ryan, G.R., Hapel, A.J., Dominguez, M.G., Russell, R.G., Kapp, S., Sylvestre, V., and Stanley, E.R. (2002). Targeted disruption of the mouse colony-stimulating factor 1 receptor gene results in osteopetrosis, mononuclear phagocyte deficiency, increased primitive progenitor cell frequencies, and reproductive defects. Blood *99*, 111–120. https://doi.org/10.1182/blood.v99.1.111.

64. Narita, K., and Takeda, S. (2015). Cilia in the choroid plexus: their roles in hydrocephalus and beyond. Front. Cell. Neurosci. *9*, 39. https://doi.org/10.3389/fncel.2015.00039.

65. Xu, H., Fame, R.M., Sadegh, C., Sutin, J., Naranjo, C., Naranjo, C., Cui, J., Shipley, F.B., Vernon, A., Gao, F., et al. (2021). Choroid plexus NKCC1 mediates cerebrospinal fluid clearance during mouse early postnatal development. Nat. Commun. *12*, 447. https://doi.org/10.1038/s41467-020-20666-3.

66. Lehtinen, M. (2019). Regulation of brain development by the choroid plexus and cerebrospinal fluid. FASEB J. *33*, 208.1. https://doi.org/10.1096/fasebj.2019.33.1_supplement.208.1.

67. Thomas, J., Morlé, L., Soulavie, F., Laurençon, A., Sagnol, S., and Durand, B. (2010). Transcriptional control of genes involved in ciliogenesis: a first step in making cilia. Biol. Cell *102*, 499–513. https://doi.org/10.1042/BC20100035.

68. Liu, M., Guan, Z., Shen, Q., Lalor, P., Fitzgerald, U., O'Brien, T., Dockery, P., and Shen, S. (2016). Ulk4 Is Essential for Ciliogenesis and CSF Flow. J. Neurosci. *36*, 7589–7600. https://doi.org/10.1523/JNEUROSCI.0621-16.2016.

69. McKenzie, C.W., Craige, B., Kroeger, T.V., Finn, R., Wyatt, T.A., Sisson, J.H., Pavlik, J.A., Strittmatter, L., Hendricks, G.M., Witman, G.B., et al. (2015). CFAP54 is required for proper ciliary motility and assembly of the central pair apparatus in mice. Mol. Biol. Cell *26*, 3140–3149. https://doi.org/10.1091/mbc.E15-02-0121.

70. Abdelhamed, Z., Vuong, S.M., Hill, L., Shula, C., Timms, A., Beier, D., Campbell, K., Mangano, F.T., Stottmann, R.W., and Goto, J. (2018). A mutation in Ccdc39 causes neonatal hydrocephalus with abnormal motile cilia development in mice. Development *145*, dev154500. https://doi.org/10.1242/dev.154500.

71. Solár, P., Zamani, A., Kubíčková, L., Dubový, P., and Joukal, M. (2020). Choroid plexus and the blood–cerebrospinal fluid barrier in disease. Fluids Barriers CNS *17*, 35. https://doi.org/10.1186/s12987-020-00196-2.

72. Yang, J., Dombrowski, S.M., Deshpande, A., Krajcir, N., and Luciano, M.G. (2010). VEGF/VEGFR-2 changes in frontal cortex, choroid plexus, and CSF after chronic obstructive hydrocephalus. J. Neurol. Sci. *296*, 39–46. https://doi.org/10.1016/j.jns.2010.06.012.

73. Praetorius, J., and Damkier, H.H. (2017). Transport across the choroid plexus epithelium. Am. J. Physiol., Cell Physiol. *312*, C673–C686. https://doi.org/10.1152/ajpcell.00041.2017.

74. Mehrad, B., Keane, M.P., and Strieter, R.M. (2007). Chemokines as mediators of angiogenesis. Thromb. Haemost. *97*, 755–762. https://doi.org/10.1160/TH07-01-0040.

75. Ohneda, O., Ohneda, K., Arai, F., Lee, J., Miyamoto, T., Fukushima, Y., Dowbenko, D., Lasky, L.A., and Suda, T. (2001). ALCAM (CD166): its role in hematopoietic and endothelial development. Blood *98*, 2134–2142. https://doi.org/10.1182/blood.V98.7.2134.

76. Bussolino, F., Di Renzo, M.F., Ziche, M., Bocchietto, E., Olivero, M., Naldini, L., Gaudino, G., Tamagnone, L., Coffer, A., and Comoglio, P.M. (1992). Hepatocyte growth factor is a potent angiogenic factor which stimulates endothelial cell motility and growth. J. Cell Biol. *119*, 629–641. https://doi.org/10.1083/jcb.119.3.629.

77. Rodríguez-Manzaneque, J.C., Fernández-Rodríguez, R., Rodríguez-Baena, F.J., and Iruela-Arispe, M.L. (2015). ADAMTS proteases in vascular biology. Matrix Biol. *44–46*, 38–45. https://doi.org/10.1016/j.matbio.2015.02.004.

78. Chen, Y., Zhou, Y., Bai, Y., Jia, K., Zhang, H., Chen, Q., Song, M., Dai, Y., Shi, J., Chen, Z., et al. (2025). Macrophage-derived CTSS drives the age-dependent disruption of the blood-CSF barrier. Neuron *113*, 1082–1097.e8. https://doi.org/10.1016/j.neuron.2025.01.023.

79. Graves, S.I., Meyer, C.F., Jeganathan, K.B., and Baker, D.J. (2025). p16-expressing microglia and endothelial cells promote tauopathy and neurovascular abnormalities in PS19 mice. Neuron *113*, 2251–2264.e4. S0896-6273(25)00303-4. https://doi.org/10.1016/j.neuron.2025.04.020.

80. Musi, N., Valentine, J.M., Sickora, K.R., Baeuerle, E., Thompson, C.S., Shen, Q., and Orr, M.E. (2018). Tau protein aggregation is associated with cellular senescence in the brain. Aging Cell *17*, e12840. https://doi.org/10.1111/acel.12840.

81. Zhang, P., Kishimoto, Y., Grammatikakis, I., Gottimukkala, K., Cutler, R.G., Zhang, S., Abdelmohsen, K., Bohr, V.A., Misra Sen, J., Gorospe, M., et al. (2019). Senolytic therapy alleviates Aβ-associated oligodendrocyte progenitor cell senescence and cognitive deficits in an Alzheimer's disease model. Nat. Neurosci. *22*, 719–728. https://doi.org/10.1038/s41593-019-0372-9.

82. Grosse, L., Wagner, N., Emelyanov, A., Molina, C., Lacas-Gervais, S., Wagner, K.-D., and Bulavin, D.V. (2020). Defined p16High Senescent

Please cite this article in press as: Watson et al., Persistent and transient senescent cells contribute to brain-barrier development, Cell (2026), https://doi.org/10.1016/j.cell.2026.05.022

Cell Types Are Indispensable for Mouse Healthspan. Cell Metab. *32*, 87–99.e6. https://doi.org/10.1016/j.cmet.2020.05.002.

83. Corliss, B.A., Doty, R.W., Mathews, C., Yates, P.A., Zhang, T., and Peirce, S.M. (2020). REAVER: A program for improved analysis of high-resolution vascular network images. Microcirculation *27*, e12618. https://doi.org/10.1111/micc.12618.
84. Love, M.I., Huber, W., and Anders, S. (2014). Moderated estimation of fold change and dispersion for RNA-seq data with DESeq2. Genome Biol. *15*, 550. https://doi.org/10.1186/s13059-014-0550-8.
85. Kinsella, R.J., Kähäri, A., Haider, S., Zamora, J., Proctor, G., Spudich, G., Almeida-King, J., Staines, D., Derwent, P., Kerhornou, A., et al. (2011). Ensembl BioMarts: a hub for data retrieval across taxonomic space. Database *2011*, bar030. Oxford. https://doi.org/10.1093/database/bar030.
86. Hao, Y., Stuart, T., Kowalski, M.H., Choudhary, S., Hoffman, P., Hartman, A., Srivastava, A., Molla, G., Madad, S., Fernandez-Granda, C., et al. (2024). Dictionary learning for integrative, multimodal and scalable single-cell analysis. Nat. Biotechnol. *42*, 293–304. https://doi.org/10.1038/s41587-023-01767-y.
87. Moreau, M.X., Saillour, Y., Elorriaga, V., Bouloudi, B., Delberghe, E., Deutsch Guerrero, T., Ochandorena-Saa, A., Maeso-Alonso, L., Marques, M.M., Marin, M.C., et al. (2023). Repurposing of the multiciliation gene regulatory network in fate specification of Cajal-Retzius neurons. Dev. Cell *58*, 1365–1382.e6. https://doi.org/10.1016/j.devcel.2023.05.011.
88. Moore, S.A., and Iulianella, A. (2021). Development of the mammalian cortical hem and its derivatives: the choroid plexus, Cajal-Retzius cells and hippocampus. Open Biol. *11*, 210042. https://doi.org/10.1098/rsob.210042.
89. Iskusnykh, I.Y., Fattakhov, N., Li, Y., Bihannic, L., Kirchner, M.K., Steshina, E.Y., Northcott, P.A., and Chizhikov, V.V. (2023). Lmx1a is a master regulator of the cortical hem. eLife *12*, e84095. https://doi.org/10.7554/eLife.84095.
90. Nowak-Sliwinska, P., Alitalo, K., Allen, E., Anisimov, A., Aplin, A.C., Auerbach, R., Augustin, H.G., Bates, D.O., van Beijnum, J.R., Bender, R.H.F., et al. (2018). Consensus guidelines for the use and interpretation of angiogenesis assays. Angiogenesis *21*, 425–532. https://doi.org/10.1007/s10456-018-9613-x.
91. Xie, Z., Niu, L., Du, K., Chen, L., Zheng, G., Dai, S., Dan, H., Duan, L., Dou, X., Feng, F., et al. (2024). Endothelial cell heterogeneity in colorectal cancer: tip cells drive angiogenesis. Cell. Mol. Life Sci. *81*, 365. https://doi.org/10.1007/s00018-024-05411-z.
92. Ashburner, M., Ball, C.A., Blake, J.A., Botstein, D., Butler, H., Cherry, J.M., Davis, A.P., Dolinski, K., Dwight, S.S., Eppig, J.T., et al. (2000). Gene ontology: tool for the unification of biology. Nat. Genet. *25*, 25–29. https://doi.org/10.1038/75556.
93. Aleksander, S.A., Balhoff, J., Carbon, S., Cherry, J.M., Drabkin, H.J., Ebert, D., Feuermann, M., Gaudet, P., Harris, N.L., Hill, D.P., et al. (2023). The Gene Ontology knowledgebase in 2023. Genetics *224*, iyad031. https://doi.org/10.1093/genetics/iyad031.
94. Wei, T., and Simko, V. (2024). corrplot: Visualization of a Correlation Matrix, [Version 0.95].

Please cite this article in press as: Watson et al., Persistent and transient senescent cells contribute to brain-barrier development, Cell (2026), https://doi.org/10.1016/j.cell.2026.05.022

STAR★METHODS

KEY RESOURCES TABLE

REAGENT or RESOURCE	SOURCE	IDENTIFIER
Antibodies		
Rabbit anti-p21	Abcam	Cat# ab188224, RRID:AB_2734729
Mouse anti-Reelin	Millipore	Cat# MAB5364, RRID:AB_2179313
Guinea pig anti-Tbr1	Synaptic Systems	Cat# 328 005, RRID:AB_2620072
Mouse anti-Aqp1	Santa Cruz Biotechnologies	Cat# sc-32737, RRID:AB_626693
Goat anti-Dll4	R&D Systems	Cat# AF1389, RRID: AB_354770
Goat anti-Cd31	R&D Systems	Cat# AF3628, RRID: AB_2161028
Rat anti-Cd31	BD Biosciences	Cat# 550274, RRID: AB_393571
Guinea pig anti-Iba1	Synaptic Systems	Cat# 234 308, RRID: AB_2924932
Goat anti-Cd206	R&D Systems	Cat# AF2535, RRID: AB_2063012
Lycopersicon Esculentum (Tomato) Lectin (LEL, TL), DyLight 594	Vector Laboratories	Cat# DL1177, RRID: AB_2336416
Lycopersicon Esculentum (Tomato) Lectin (LEL, TL), DyLight 649	Vector Laboratories	Cat# DL1178
Rat anti-Ki67-APC	Thermo Fisher Scientific	Cat# 17-5698-80, RRID: AB_2688056
Rabbit anti-Collagen IV	Novus Biologicals	Cat# NB1206586, RRID: AB_789360
Goat anti-Laminin α4	R&D Systems	Cat# AF3837, RRID: AB_2249744
Mouse anti-phospho-H2A.X (S139)	Millipore	Cat# 05-636, RRID: AB_309864
Rabbit anti-ERG	Cell Signaling	Cat# 97249, RRID: AB_2721841
Rat anti-mCherry	Invitrogen	Cat# M11217, RRID: AB_2536611
Rabbit anti-p7S3	Abcam	Cat# ab776999, RRID: AB_776999
Rat anti-Ter119	R&D Systems	Cat# MAB1125, RRID: AB_2297123
Rabbit anti-Tbr2	Abcam	Cat# ab216870, RRID: AB_2943124
Goat anti-Sox2	R&D Systems	Cat# AF2018, RRID: AB_355110
Rabbit anti-ZO-1	Invitrogen	Cat# 617300, RRID: AB_138452
Sheep anti-Plxnb2	R&D Systems	Cat# AF5329, RRID: AB_2166425
Rat anti-Integrin β1 (Cd29)	BD Biosciences	Cat# 550531, RRID: AB_393729
Chemicals, peptides, and recombinant proteins		
Tamoxifen	Sigma	Cat# T5648
EdU	Invitrogen	Cat# A10044
O-Propargyl-Puromycin (OPP)	MedChemExpress	Cat# HY-15680
32% Paraformaldehyde	Electron Microscopy Sciences	Cat# 15714-S
Fluoromount-G	Electron Microscopy Sciences	Cat# 17984-25
Critical commercial assays		
CellEvent™ Senescence Green Detection Kit	Invitrogen	Cat# C10850, RRID: SCR_018827
TUNEL	Roche	Cat# 11684795910
Click-iT™ EdU Cell Proliferation Kit for Imaging, Alexa Fluor™ 488 dye	Invitrogen	Cat# C10337
Click-iT™ Plus OPP Alexa Fluor™ 488 Protein Synthesis Assay Kit	Invitrogen	Cat# C10456
Deposited Data		
Mouse embryonic brain single-cell RNA-seq	La Manno et al.[25]	SRA: PRJNA637987
Embryonic endothelial cell single-cell RNA-seq	Chen et al.[56]	GEO: GSE216970

(*Continued on next page*)

Please cite this article in press as: Watson et al., Persistent and transient senescent cells contribute to brain-barrier development, Cell (2026), https://doi.org/10.1016/j.cell.2026.05.022

Continued

REAGENT or RESOURCE	SOURCE	IDENTIFIER
Experimental models: Organisms/strains		
B6.Cg-Gt(ROSA)26Sor$^{tm9(CAG-tdTomato)Hze}$/J	JAX Mice and Services	RRID: IMSR_JAX:007909
B6.129P2-Gt(ROSA)26Sor$^{tm1(DTA)Lky}$/J	JAX Mice and Services	RRID: IMSR_JAX:009669
B6.Cg-Csf1r$^{tm1.2Jwp}$/J	JAX Mice and Services	RRID: IMSR_JAX:021212
Oligonucleotides		
sgRNA to generate p21-CreERT2: GACATCACCAGGATTGGACA	This paper	N/A
Primers for Cre genotyping: F: TGACCAGAGTCATCCTTAGCG; R: AATGCTTCTGTCCGTTTGCC	This paper	N/A
Primers for p21 genotyping: F: CATGGTGTGGTGGAAAAGCA; R: AGAGACAACGGCACACTTTG	This paper	N/A
Software and algorithms		
Fiji/ImageJ	ImageJ	RRID: SCR_002285
NIS Elements Imaging Software	Nikon	https://www.microscope.healthcare.nikon.com/products/software/nis-elements
R	R Core Team	https://r-project.org/
Seurat v5	Hao et al.[86]	RRID: SCR_016341
Cell Ranger	10× Genomics	RRID: SCR_017344
DESeq2	Love et al.[84]	https://bioconductor.org/packages/release/bioc/html/DESeq2.html
corrplot	Wei and Simko[94]	https://github.com/taiyun/corrplot
Horos	Horos Project	Horosproject.org
GraphPad Prism	GraphPad	RRID: SCR_002798

EXPERIMENTAL MODEL AND STUDY PARTICIPANT DETAILS

Mice

All animal procedures were carried out in accordance with NIH guidelines and approved by the University of California, San Diego Institutional Animal Care and Use Committee. Animals were maintained in a pathogen-free vivarium on a 12 h:12 h light:dark cycle (light on: 6:00 am – 6:00pm) with food and water ad libitum. Vivarium temperature was maintained between 18 and 23C and humidity between 40% and 60%. Animals were group housed and experimental animals were drug- and procedure naïve prior to use in this study except for the experimental manipulations described below. Mice of both sexes were used for experiments. Pregnant Swiss-Webster mice were purchased from Charles River Laboratories. Ai9 (JAX#007909), iDTA (JAX#009669), and Csf1r$^{flox/flox}$ (JAX#021212) mice were purchased from Jackson Laboratories. *Cdkn1a*^{CreERT2} mice were generated by microinjection of donor template (Integrated DNA Technologies) and Cas9 protein (Integrated DNA Technologies) complexed with single guide RNA (sgRNA, Integrated DNA Technologies) targeting the *Cdkn1a/p21* promoter into pronuclear stage embryos (C57BL/6NHsd) that were implanted into a foster female. sgRNA sequence information can be found in key resources table.

Mouse genotype was confirmed by PCR using primer pairs provided by Jackson Laboratories with the exception of *Cdkn1a*^{CreERT2} mice, which were genotyped using Cre primers and custom primers to differentiate between homozygous and heterozygous copies of the CreERT cassette (Key resources table).

For timed pregnancy, the morning that vaginal plugs were detected was considered E0.5. 5-ethynyl-2'-deoxyuridine (EdU; Invitrogen) and O-propargyl-puromycin (OPP; Invitrogen) incorporation assays were performed by intraperitoneal (IP) injection of pregnant dams with EdU (10mM, Invitrogen) or OPP (50 mg/kg, MedChemExpress) for 1 h prior to embryo collection. For tamoxifen labeling experiments, tamoxifen (Sigma, T5648) was prepared in 100% ethanol solution (20 mg/mL) and stored at -20°C. Prior to use, 400 μL corn oil (Sigma, C8257) was added and the solution was placed at 65°C to evaporate ethanol for 1 – 2 h. 150 μL of tamoxifen in corn oil was injected into pregnant dams (~25 mg/kg) in the late afternoon ~16:00. A high proportion (> 95%) of pregnant dams administered tamoxifen during the gestational period experienced difficulty giving birth (dystocia). To overcome this and examine postnatal offspring, terminal C-sections were performed at E19.5 and embryos were transferred to foster female mice (BALB/c) with recently born litters (P1 - 5).

Please cite this article in press as: Watson et al., Persistent and transient senescent cells contribute to brain-barrier development, Cell (2026), https://doi.org/10.1016/j.cell.2026.05.022

For DTA and Csf1r$^{flox/flox}$ experiments, control littermates (Cre^{-}iDTA^{+} or Cre^{-}Csf1r$^{flox/flox}$) were used to account for tamoxifen toxicity and transgene leakiness. To assess hemorrhage frequency, we developed a qualitative 5-point scale where 0 represents no hemorrhage (visibly clear brains) and 5 indicates extensive hemorrhage with blood pooling within brain tissue.

METHOD DETAILS

Tissue collection and processing for immunostaining and histology

Adult mice were given a lethal dose of anesthetic (isoflurane overdose) followed by transcardial perfusion with PBS (pH 7.4) followed by PBS with 4% paraformaldehyde (Electron Microscopy Sciences, 15714). Pregnant dams were euthanized by isoflurane overdose or carbon dioxide asphyxiation. Whole embryos (E10.5 – E14.5) or dissected brains (E15.5 – PND21) were drop fixed in 4% PFA for 24 – 48 h prior to dehydration in 30% sucrose until tissue sank. Tissue was cryopreserved in optimal cutting temperature (O.C.T) compound (Tissue-Tek) and cryosectioned (Epredia NX70) in sagittal or coronal orientation at 20 μm thickness directly onto microscope slides. Tissue was dried on slides for 1 – 2 h or overnight and stored in slide boxes with desiccant at -20C. In some cases, adult brain tissue was sectioned using a vibratome (Leica VT1000 S) at 40 μm thickness. Free-floating sections were stored in PBS/0.02% sodium azide at 4C.

Immunostaining and histology

For immunostaining, cryosections were incubated with primary antibody diluted in PBS/0.3% Triton-X 100 (in some cases, 5% normal donkey serum was used as a blocking agent) overnight at 4°C, washed in PBS, and incubated with secondary antibody for 1 – 2 h at room temperature in the dark. Free-floating sections were incubated with primary antibody for 48 h. Sections were counterstained with DAPI (Sigma) and mounted with Fluromount-G (Invitrogen). For SA-β-gal detection, immunostaining was performed first followed by incubation with CellEvent™ Senescence probe (C10850) at 37°C for 3 h. Terminal deoxynucleotidyl transferase-mediated dUTP-X nick end labeling (TUNEL) staining was performed prior to immunostaining according to manufacturer's instructions (Roche, 11684795910). For EdU detection, Click-iT™ EdU Cell Proliferation Kit for Imaging, Alexa Fluor™ 488 dye (C10337) was used according to manufacturer's instructions. For OPP, Click-iT™ Plus OPP Alexa Fluor™ 488 Protein Synthesis Assay Kit (C10456) was used according to manufacturer's instructions, with antibody staining following the Click-iT reaction. Some antibodies (γH2AX and Reln) required antigen retrieval prior to detection for optimal signal. Briefly, tissue sections (cryosections or free-floating) were incubated in 1X citrate buffer (pH 6.0, Sigma) at 90 – 95°C for 20 minutes prior to immunostaining. Nissl staining was performed by incubating cryosections in 0.1% cresyl violet for 8 minutes prior to dehydration and mounting. Lipofuscin detection was performed using an optimized Sudan Black B protocol [37] with minor modifications, including an incubation time of 30 minutes followed by extensive washing prior to primary antibody incubation.

Confocal imaging and analysis

A Nikon AX confocal microscope with 4X (air), 20X (air), and 60X (oil immersion medium) objectives and NIS Elements Imaging Software were used for all imaging acquisition. Identical imaging settings were used for all comparative experiments. Image processing and analysis was performed using Fiji image processing software (ImageJ). For quantification, desired regions were cropped in Fiji and run through pre-built macros. At least 2 – 5 images per region per biological replicate were averaged for each representative data point. Unless otherwise specified, collapsed z-projections of identical distance and number per condition were used for image analysis.

p21 and SA-β-gal quantification

Images were cropped by DAPI staining morphology to contain only regions of interest, using the Developing Mouse Brain reference atlas from Allen Brain Institute (developingmouse.brain-map.org) as a guide. For SA-β-gal quantification, DAPI and SA-β-gal were thresholded to create binary images of each stain. The area of each channel was then measured; DAPI area was used to normalize SA-β-gal area for each image. For p21 quantification, p21 was thresholded, watershed, and p21^{+} cells were counted using the analyze particles function in Fiji.

tdTomato quantification

For the whole brain tdTomato (tdT) region analysis, the brain was manually divided into 11 regions: the cerebellum, 4V choroid plexus, hindbrain, midbrain, hypothalamus, thalamus, hippocampus, cortex, olfactory bulb, cerebral nuclei, and LV choroid plexus. DAPI and tdT were thresholded to create binary images. The area of each channel was then measured and the DAPI area was used to normalize tdT area for each image.

Vascular cells

In the Cd31 or Lectin channel, the subtract background and despeckle functions were used to denoise images. The channel was then thresholded to create a binary mask and the area was taken. tdT was thresholded to create a binary mask that was overlaid onto the Cd31 or Lectin mask such that only Cd31 or Lectin that overlapped with tdT remained (Cd31^{+}/tdT^{+} or Lectin^{+}/tdT^{+} area). Cd31^{+}/tdT^{+} or Lectin^{+}/tdT^{+} as a percentage of total Cd31^{+} or Lectin^{+} area was calculated and presented as a histogram.

Please cite this article in press as: Watson et al., Persistent and transient senescent cells contribute to brain-barrier development, Cell (2026), https://doi.org/10.1016/j.cell.2026.05.022

Macrophage cells

DAPI, Iba1, and tdT were thresholded to create binary masks of each channel. Iba1 was then masked by DAPI, such that only the Iba1$^+$ nucleus remained. The Iba1$^+$ nuclei were counted using analyze particles and a mask was produced that was subsequently masked by tdT$^+$ cells such that only Iba1$^+$/tdT$^+$ nuclei remained for quantification using analyze particles. Iba1$^+$/tdT$^+$ cells as a percentage of total Iba1$^+$ cells was calculated and presented as a histogram.

Choroid Plexus

Images were cropped to only contain AQP1$^+$ choroid plexus tissue. DAPI and tdT were thresholded to create binary mask images. DAPI area was measured and used to mask tdT, so only tdT that overlapped with DAPI remained to quantify tdT$^+$ (% DAPI area).

CR cells

p73 and tdT were thresholded to create a binary mask image. PND21 p73 staining had higher background than at E18.5, so prior to thresholding, the subtract background function was used for PND21 images. Additionally, as there were many more closely packed p73$^+$ cells at E18.5, watershedding was applied to the p73 binary mask. p73$^+$ cells were counted using analyze particles and applied to tdT to determine p73$^+$/tdT$^+$ cells, which were presented as a proportion of total p73$^+$ cells.

Quantification in p21$^+$ and p21$^-$ cells

DAPI, p21, and the other channel (Ki67, TUNEL, γH2AX, OPP) were initially thresholded to create a binary image of each stain. The p21$^+$ binary image was then duplicated and inverted to create a p21$^-$ binary image. DAPI was masked by the p21$^+$ binary image and the number of p21$^+$ cells were counted using analyze particles. A copy of the initial DAPI mask was masked by the p21$^-$ binary image and the number of p21$^-$ cells were counted using analyze particles. For Ki67 quantification, the counted particles (p21$^+$ or p21$^-$) were then masked by Ki67 to determine p21$^+$/Ki67$^+$ and p21$^-$/Ki67$^+$ cells. The proportion of cells that were Ki67$^+$ was calculated by dividing the p21$^+$/Ki67$^+$ or p21$^-$/Ki67$^+$ count by the p21$^+$ or p21$^-$ cell count, respectively. For TUNEL, γH2AX, and OPP, a similar pipeline was used, however, the intensity (mean gray value) of those signals were quantified in p21$^+$ and p21$^-$ cells, and the relative intensity was determined by dividing the average p21$^+$ signal intensity by the average p21$^-$ signal intensity per image.

Ki67 quantification of tdT$^+$ and tdT$^-$ cells

In ROI of identical size (for forebrain and hindbrain) or cropped LV and 4V ChP, DAPI, tdT, and Ki67 was thresholded to create binary mask images. Ki67$^+$ cells that overlapped with tdT$^+$/DAPI$^+$ signal or with tdT$^-$/DAPI$^+$ signal were identified and the proportion of Ki67$^+$/tdT$^-$ or Ki67$^+$/tdT$^+$ cells relative to DAPI area were scored and presented in histogram format. Since Ki67$^+$ cells were rare in ChP tissue, adjacent forebrain or hindbrain proliferation indices were used for comparison.

Iba1$^+$/tdT$^+$ and *Iba1$^+$/tdT$^-$ distance to tdT$^+$ vasculature quantification*: Iba1$^+$/tdT$^+$ and Iba1$^+$/tdT$^-$ brain-resident macrophages were identified and the distance from the Iba1$^+$ signal to the closest tdT$^+$ blood vessel (identified by tdT morphology) was quantified using the line function.

Blood vessel morphology analysis

Blood vessel quantification was accomplished by analyzing Cd31 signal using the REAVER analysis program.[83] Specifically, images were pre-processed in ImageJ to crop to identical ROI and binarized. These images were then analyzed in REAVER using the following parameters: an averaging filter size of 200 pixels to smooth the image and enhance larger structures, a minimum connected component area of 100 pixels to filter out small, irrelevant details while still capturing smaller vessel portions, a wire dilation parameter of 0 to focus solely on existing features, and a vessel thickness threshold of 2 to accurately identify and analyze vessel-like structures. Measurements for vessel area fraction, vessel length, vessel diameter, number of branchpoints, number of segments, and valency for all samples were recorded.

Laminin α4, and Collagen IV intensity in Cd31$^+$ blood vessels

Regions were cropped to identical ROI and the Cd31 channel was used to generate a mask under which mean Laminin α4 and Collagen IV signal intensity were measured.

Cresyl violet quantifications

For measurements of cortical length, midbrain length, cerebellum length, whole brain length, hippocampal area, LV and 4V ChP length, and LV area, cresyl violet-stained sections were imaged and the freehand selection (ventricle and hippocampal area) or line tools (all other measurements) in imageJ were used.

Progenitor cell quantifications (*DAPI cortical layers, Sox2 and Tbr2 in cortex and hippocampus*): Cortical images were rotated such that the ventricular zone was parallel to the bottom of the image and identical regions of 300 μm in width were cropped. Based on DAPI morphology, the ventricular/subventricular zone (VZ/SVZ), intermediate zone (IZ), subplate (SP), cortical plate (CP) and marginal zone (MZ) were measured using the line tool in imageJ. For Tbr2 and Sox2 area in the cortex, both channels were thresholded

Please cite this article in press as: Watson et al., Persistent and transient senescent cells contribute to brain-barrier development, Cell (2026), https://doi.org/10.1016/j.cell.2026.05.022

to generate binary masks. Then, the area of Tbr2$^+$ or Sox2$^+$ signal was quantified and divided by the total cortical length. For Tbr2 quantification in the suprapyramidal and infrapyramidal layers of the hippocampus, those regions were cropped and Tbr2$^+$ cells were manually scored.

Signal intensity (Aqp1, Plxnb2, Integrin β1) and Cd31 area in the ChP

LV ChP structures were cropped based on DAPI morphology using the freehand selection tool in imageJ. DAPI was thresholded to generate a binary mask, and the total DAPI area per ChP was quantified. Mean signal intensity was calculated per ChP image and divided by the total DAPI area per ChP image to obtain a mean intensity per ChP area. For Cd31 area, Cd31 was thresholded to generate a binary image and Cd31 area was quantified and divided by the total DAPI area of the ChP to obtain Cd31$^+$ area (% LV ChP area).

Bulk and single-cell RNA-sequencing analysis

Bulk RNA-sequencing analysis to identify SaTS and SASP

RNA-sequencing data generated by Sturmlechner et al.[32] and Marin et al.[33] was obtained from the Gene Expression Omnibus under accession GSE117278 and GSE202032. Differential expression analysis was performed using DESeq2.[84] Genes were considered significantly differentially expressed if they had a p.adj. < 0.05 and |log2FC| > 0.3. To identify SaTS, we intersected the up- and down-regulated DEG lists and extracted genes that were shared across all four *in vitro* senescence models. To identify SASP, secreted factors[38] were extracted from genes upregulated in at least one mode of senescence (DOX, IR, OIS, REP).

We compared SaTS to senescence gene sets identified in two independent studies.[34,35] For the cellular senescence signature identified in Chatsirisupachai et al., human genes were converted to mouse using BioMart.[85] For SenMayo, the mouse gene list was used.

Single-cell RNA-sequencing analysis: Read alignment and data processing

Single-cell RNA-sequencing data generated by La Manno et al.[25] was obtained in FASTQ format from the Sequence Read Archive (SRA) under accession PRJNA637987. FASTQs were run through Cell Ranger (v7.2.0) to align reads to the mouse genome (mm10) and generate feature-barcode matrices. Resulting matrices were input into the R program Seurat (v5.3.0)[86] and merged into a Seurat object. Cells with fewer than 2,000 unique molecular identifiers (UMIs) or mitochondrial DNA exceeding 5% were excluded from the dataset, resulting in a final Seurat object of 283,323 cells. Normalization, feature selection (2,500 features), data scaling and linear dimensionality reduction (PCA) were performed following the standard Seurat workflow. Batch correction was applied using the Harmony algorithm (https://github.com/immunogenomics/harmony) using the 'batch' designation in the sample metadata.[25] Clustering and Uniform Manifold Approximation and Projection (UMAP) were performed on batch-corrected data. We ran 'Find all markers' to identify highly expressed transcripts in each cluster (Table S1) and manually annotated and curated the clusters with respect to major class, subclass, and spatial location using the previously published dataset[25] as a guide (Table S2).

Single-cell RNA-sequencing analysis: Differential expression analysis

The single-cell dataset was subset into two groups based on *Cdkn1a*/p21 expression level: p21$^+$ cells (75th percentile, normalized expression = 1.484812) and *p21*$^-$ cells (normalized expression = 0). Aggregate count matrices were generated for each sample in each group (p21$^+$ and p21$^-$) by averaging expression of each gene across all cells within a sample (original 10X run). Differential expression analysis was subsequently conducted using DESeq2,[84] with each sample serving as a biological replicate. For differential expression analysis of specific clusters, the corresponding UMAP cluster was isolated (using ''subset'' in Seurat) followed by separation of p21$^+$ (75th percentile, normalized expression = 1.818654 (cluster21), 1.926037 (cluster22), 1.478045 (cluster31), and 2.364703 (cluster39)) and *p21*$^-$ (expression = 0) and assigned to 'pseudoreplicates' ($n = 3$) to serve as biological replicates, as splitting by original sample resulted in too few cells per replicate. A subset of cluster 31 cells resembled neuronal cells (*Tubb3, Eomes/Tbr2, Reln, Tbr1, NeuroD1/2*), therefore to gain insight into the ChPe-specific p21$^+$ signature, we removed that subcluster from ChPe analysis. ChPe and CR cells arise from roof plate neuroepithelial cells.[41,87–89] We identified a presumptive ChPe and CR progenitor cell cluster (cluster35) based on marker gene expression (*Rspo1/2/3, Lmx1a, Msx1, Id1/3, Hes1, Wnt1, Wnt3a*).[24] Genes were considered differentially expressed if they had a p.adj. < 0.05 and |log2FC| > 0.3 (at least 10 normalized counts in any pseudoreplicate).

Single-cell RNA-sequencing analysis: Analysis of endothelial tip cells

The vascular endothelial cell cluster (cluster 21) of the La Manno et al. dataset was isolated and tip cells were identified using 'AddModuleScore' (*Dll4, Esm1, Kdr, Angpt2, Cxcr4*, and *Apln*[90,91] with 90th percentile score threshold). Differential expression analysis was performed using the strategy described above in tip and non-tip (all other endothelial) cells. To expand the dataset to non-CNS populations, we used single-cell RNA-sequencing data of endothelial cells isolated from multiple embryonic (E9.5, E12.5, and E15.5) organs including brain, heart, lung, liver, kidney, and small intestine[56] (GSE216970) processed in Seurat (v5.3.0).[86] Normalization, feature selection (2,500 features), data scaling and linear dimensionality reduction (PCA) were performed following the standard Seurat workflow. Samples were integrated with the anchor-based CCA workflow to correct for batch effects, followed by clustering and UMAP visualization. Endothelial cells were isolated using FeaturePlot inspection and marker-based annotation (*Etv2, Pecam1, Cdh5*). Brain endothelial cells were isolated using 'AddModuleScore' (*Slc38a5, Tfrc, Slc7a5, Mfsd2a, Tgfb, Gkn3*) and by matching the reported 1,024 cell endothelial cluster.[56] Tip cell identification, p21$^+$ classification, and differential expression analysis were performed as described above, with tip cells compared to p21$^-$ non-tip cells in each group. A Fisher's exact test was used to determine statistical significance in p21$^+$ population enrichment.

Gene ontology analysis

Gene ontology analysis was performed using either a custom in-house analysis pipeline or GO_{RILLA} with two unranked lists of genes (target and background lists) followed by REViGO visualization to remove redundant GO terms and generate a scatterplot with unbiased reduction of GO terms in semantic space (*x, y*). For custom analysis, genes annotated to specific GO categories were isolated from the Gene Ontology Resource[92,93] and randomized permutation tests were performed (see Permutation Tests in *Statistics and reproducibility*) to determine enrichment over background. An enrichment score (log_2(Obs/Exp)) *(-log(p_val)) for upregulated genes and log_2(Obs/Exp)) *(log(p_val)) for downregulated genes) was calculated for visualization. Genes expressed in the given cell type were used as background.

Receptor-ligand analysis

We compiled a list of receptor-ligand pairs from a public repository (https://github.com/LewisLabUCSD/Ligand-Receptor-Pairs)[50] and identified all receptor- and ligand-encoding genes that were upregulated in $p21^+$ VECs and macrophages. Using the curated receptor-ligand pairings, we then determined whether the upregulated ligands in one cell type had corresponding receptors upregulated in the other (and vice versa). To assess whether the observed overlap exceeded random expectation, we performed a hypergeometric test.

MRI Acquisition and Analysis

Images were acquired using a Bruker 7T 70/20 MRI scanner (Bruker, Billerica, MA) running an Avance NEO console equipped with a 72mm quadrature transmit only volume coil and a receive-only 4-channel mouse cardiac surface array coil. Samples were scanned in a 15cc conical tube with a T2-w TurboRARE MRI sequence in the Axial and Sagittal planes with the following parameters: TE/TR = 36ms/2500ms, 25 averages, RARE factor 8, matrix = 100 x 100 x 21, voxel size = 100 μm x 100 μm x 500 μm, Scan time = 12:30. MR Images were loaded into Horos (Purview, Annapolis, MD) and were manually segmented to measure ventricle volume. Left and right lateral ventricle volumes were combined. To measure relative intensity of MR signal, identical ROI within the left and right neck area were generated and the mean intensity was averaged from five sequential images.

QUANTIFICATION AND STATISTICAL ANALYSIS

Data were analyzed using GraphPad Prism version 10 unless otherwise specified. All experiments were independently replicated using biologically distinct samples. Biological replicate numbers, statistical tests, and definitions of error bars are indicated in the corresponding figure legends. Sample sizes were selected based on embryo availability, consistency with prior studies, and reproducibility across biological replicates. No data were excluded unless technical failure occurred during tissue processing, staining, imaging, or sequencing quality control as described in the relevant Method Details sections. For comparisons between two groups, data were analyzed by two-tailed Student's t-test. For comparisons between multiple groups, one-way or two-way ANOVA with multiple comparisons was used. Differences were considered statistically significant at *($P < 0.05$), **($P < 0.01$), ***($P < 0.001$), and ****($P < 0.0001$). Unless otherwise stated, all data is plotted with individual data points and the error bars represent standard deviation of the mean.

Permutation tests

Randomized permutation tests were completed using custom R scripts. Briefly, a sample set of equal size as the observed data was randomly selected from the background set and the statistic test was calculated for each randomly sampled data (s* = s1, s2, … sN) exactly as for the observed data (sObs). This was iterated N = 10^4 times with replacement to create the null distribution and the p-value was calculated using the formula: p-value = sum(s* >= sObs)/N. If sObs was greater than or less than all values in the null distribution, the p-value was set as < 1E-5. Comparisons used for all permutation tests are provided in Table S3.

Correlation analysis

For the $p21^+$ cell DEG correlations with mouse SaTS, a 10,000-iteration permutation was performed comparing all gene lists to each other. To produce a correlation matrix from these results, the log2(observed overlap/expected overlap)*-log(p-value) was calculated for each gene list comparison. To give each comparison a relative score, any results less than zero were divided by the absolute value of the minimum result for each gene list, while any results greater than zero were divided by the maximum results for each gene list. Any comparisons with a result of zero due to a 0% overlap were changed to -1 as these gene were considered inversely correlated. This matrix was input into the corrplot[94] R package (https://github.com/taiyun/corrplot) which calculated the correlation scores and produced a correlation plot.